Structure of the human epithelial sodium channel by cryo-electron microscopy

Sigrid Noreng[1], Arpita Bharadwaj[2], Richard Posert[1], Craig Yoshioka[3], Isabelle Baconguis[2]*

[1]Department of Biochemistry & Molecular Biology, Oregon Health and Science University, Portland, United States; [2]Vollum Institute, Oregon Health and Science University, Portland, United States; [3]Department of Biomedical Engineering, Oregon Health and Science University, Portland, United States

Abstract The epithelial sodium channel (ENaC), a member of the ENaC/DEG superfamily, regulates Na^+ and water homeostasis. ENaCs assemble as heterotrimeric channels that harbor protease-sensitive domains critical for gating the channel. Here, we present the structure of human ENaC in the uncleaved state determined by single-particle cryo-electron microscopy. The ion channel is composed of a large extracellular domain and a narrow transmembrane domain. The structure reveals that ENaC assembles with a 1:1:1 stoichiometry of α:β:γ subunits arranged in a counter-clockwise manner. The shape of each subunit is reminiscent of a hand with key gating domains of a 'finger' and a 'thumb.' Wedged between these domains is the elusive protease-sensitive inhibitory domain poised to regulate conformational changes of the 'finger' and 'thumb'; thus, the structure provides the first view of the architecture of inhibition of ENaC.
DOI: https://doi.org/10.7554/eLife.39340.001

Introduction

The fine-tuning of Na^+ homeostasis is largely mediated by epithelial sodium channels (ENaC) that are related in amino acid sequence to acid-sensing ion channels (ASIC) found in eukaryotes, degenerin channels (DEG) of *Caenorhabditis elegans*, and the FMRF-amide peptide-gated channels (FaNaCh) of mollusk (*Driscoll and Chalfie, 1991*; *Chalfie and Wolinsky, 1990*; *Kellenberger and Schild, 2002*; *Waldmann et al., 1997a*; *Waldmann et al., 1997b*; *Krishtal and Pidoplichko, 1981*; *Chelur et al., 2002*; *Garty and Palmer, 1997*; *Cottrell et al., 1990*; *Lingueglia et al., 1995*). These ion channels belong to the voltage-independent, Na^+-selective, and amiloride-sensitive ENaC/DEG superfamily which together perform diverse cellular functions in different organisms. In humans, ENaCs are expressed at the apical surface of epithelial tissues throughout the body, and play critical roles that range from regulation of total-body salt, water, and blood volume, to modulating airway surface liquid clearance in epithelial cells in the lungs (*Büsst, 2013*; *Ismailov et al., 1996*; *Rossier et al., 2015*; *McDonald et al., 1994*). The importance of ENaC in Na^+ homeostasis is highlighted by gain-of-function mutations causing severe hypertension, as in Liddle syndrome, or loss-of-function mutations causing the neonatal salt-wasting disorder pseudohypoaldosteronism type 1 (PHA-1) (*Gründer et al., 1997*; *Hansson et al., 1995*; *Shimkets et al., 1994*; *Chang et al., 1996*; *Edelheit et al., 2005*; *Kerem et al., 1999*). More subtle ENaC dysfunction contributes to diseases as diverse as essential hypertension, heart failure, and nephrotic syndrome (*Soundararajan et al., 2010*; *Hamm et al., 2010*; *Zheng et al., 2016*). ENaCs require three different subunits to form a functional channel, α, β, and γ (*Canessa et al., 1994*). Despite decades of study, the number of subunits in an active channel remains unclear (*Shobair et al., 2016*).

Unique among the ENaC/DEG channels, ENaCs are activated by proteolysis of peptidyl tracts embedded in the extracellular domain (ECD), which releases inhibitory peptides. The cleavage event

eLife digest The bodies of humans and other animals contain many different fluids that play vital roles in the body, such as blood, saliva and the fluids that surround cells in organs. These fluids all contain particles called ions, which can affect the flow of water into and out of cells and alter the activity of proteins. Therefore, in order to survive, an animal must tightly regulate the levels of ions in its body.

Epithelial cells line the surface of organs, and the inside of the digestive system and other cavities in the human body. A channel known as ENaC is found on the surface of epithelial cells and controls the volume of the fluid surrounding cells, blood pressure and the volume of liquid in the airways. This channel spans the membrane surrounding each epithelial cell and allows sodium ions to pass into the cell. To promote the opening of the channel, enzymes remove portions of the ENaC called extracellular domain, which sits on the outside surface of an epithelial cell. Three components (or 'subunits') called alpha, beta and gamma are needed to form an ENaC, but it is not clear how they fit together to form a single working unit.

Noreng et al. used a technique called cryo-electron microscopy to study the three-dimensional structure of the human ENaC. This revealed that a single channel contains one alpha, one beta and one gamma subunit, which sit next to each other to form a narrow tube through the membrane and a large extracellular domain. When viewed from the outside of the cell the subunits form a narrow ring in a counter-clockwise manner.

Further analysis of the structure suggested that when enzymes remove pieces of the extracellular domain of ENaC, it becomes easier for the rest of the channel to adopt a shape that allows sodium ions to move through the pore. A next step will be to study the three-dimensional structure of ENaC when it takes on different shapes to better understand how it works.

DOI: https://doi.org/10.7554/eLife.39340.002

increases channel opening probability, P_o (*Orce et al., 1980*; *Vallet et al., 1997*; *Vallet et al., 2002*; *Vuagniaux et al., 2002*; *Hughey et al., 2004*; *Hughey et al., 2003*; *Caldwell et al., 2004*; *Passero et al., 2010*; *Kleyman et al., 2009*). Amino acid sequence alignments and biochemical analyses in the ECD have so far revealed that only the β subunit lacks the characteristic motifs for protease recognition. ENaCs are widely known as substrates of serine proteases like furin, and a growing list of proteases that recognize sites in ENaC suggests a multifaceted regulation of channel function (*Rossier and Stutts, 2009*). Indeed, the complexities of ENaC function involving the requisite heteromeric subunit assembly and asymmetric subunit modification via differential proteolytic processing are critical to ion channel gating. Thus, to define subunit arrangement and stoichiometry, and elucidate the molecular architecture of ENaC inhibition, we determined the structure of ENaC in the uncleaved state by single-particle cryo-electron microscopy (cryo-EM).

Results

Design and expression of ΔENaC

We first assessed the expression of full-length (FL) ENaC by small-scale expression in adherent HEK293S GnTI⁻ cells and fluorescence-detection size-exclusion chromatography (FSEC) (*Kawate and Gouaux, 2006*). We found a low, wide peak, indicating a poorly expressing polydisperse population unsuitable for cryo-EM (*Figure 1a*). We thus screened a number of deletions and mutations in each ENaC subunit, harnessing information derived from previous biochemical and functional experiments gauging the propensity for heterotrimeric formation of ENaC and its susceptibility to proteolytic processing (*Canessa et al., 1994*; *Orce et al., 1980*; *Vallet et al., 1997*; *Vallet et al., 2002*; *Vuagniaux et al., 2002*; *Hughey et al., 2004*; *Hughey et al., 2003*; *Caldwell et al., 2004*; *Passero et al., 2010*), before arriving at the construct referred to here as ΔENaC (*Figure 1a–c*, *Figure 1—figure supplement 1*, *Figure 1—figure supplement 2*).

ΔENaC is composed of αβγ subunits truncated at the N- and C-termini (*Figure 1b,c*). Additionally, the Δα and Δγ subunits possess mutations in the identified furin and prostasin sites which prevent subunit cleavage and channel activation (*Hughey et al., 2003*; *Bruns et al., 2007*). For protein
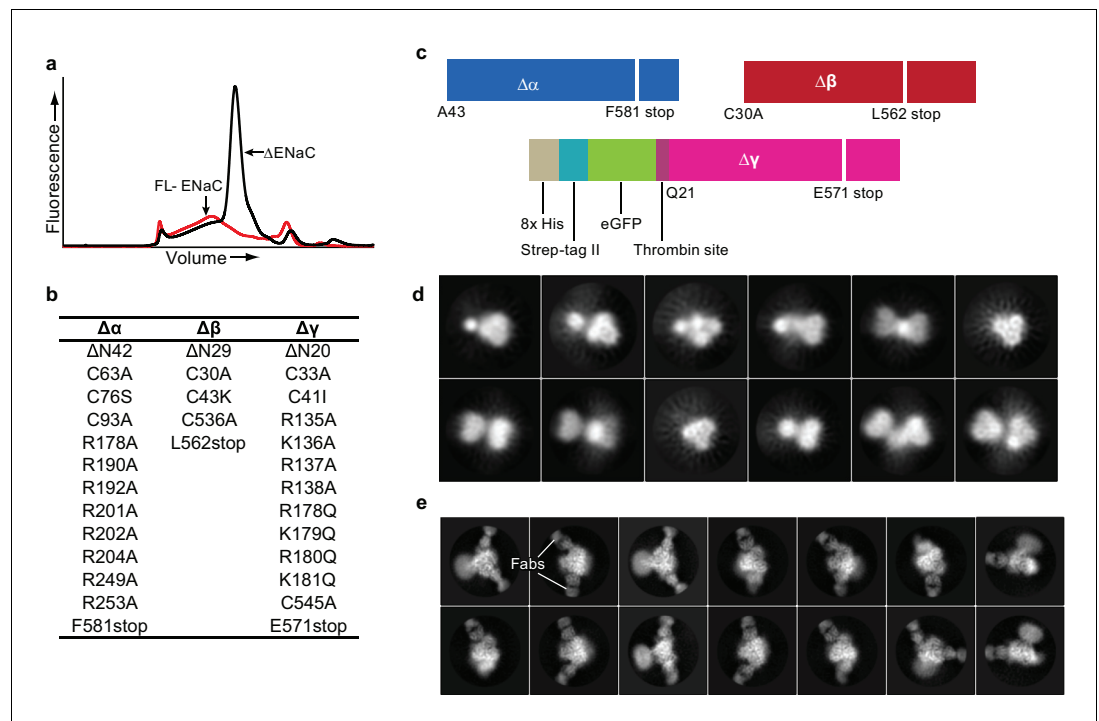
Figure 1. Creation and analysis of ΔENaC. (**a**) Representative FSEC traces of full-lenth ENaC (FL-ENaC, red) and ΔENaC (black). (**b**) Summary of mutations in ΔENaC. (**c**) Summary of ΔENaC constructs. (**d**) Representative 2D class averages of ΔENaC show that pseudosymmetry inherent in ENaC hampers particle alignment. (**e**) Representative 2D class averages of ΔENaC-7B1/10D4 complex showing increased detail due to alignment aid from Fabs.
DOI: https://doi.org/10.7554/eLife.39340.003

The following figure supplements are available for figure 1:

Figure supplement 1. Sequence alignment of ENaC with other members of the ENaC/DEG superfamily (human ENaCα residues 1-387).
DOI: https://doi.org/10.7554/eLife.39340.004

Figure supplement 2. Sequence alignment of ENaC with other members of the ENaC/DEG superfamily (human ENaCα residues 388-669)
DOI: https://doi.org/10.7554/eLife.39340.005

Figure supplement 3. Fab generation.
DOI: https://doi.org/10.7554/eLife.39340.006

Figure supplement 4. Fab binding properties.
DOI: https://doi.org/10.7554/eLife.39340.007

purification, neither Δα nor Δβ were modified with affinity tags because there is strong evidence that the α subunit can readily form functional homomeric channels, and the termini of Δβ are sensitive to perturbations (*Canessa et al., 1993*). As a result, Δγ contains both GFP and a Strep-II tag at the N-terminus (*Figure 1c*), minimizing contamination by homomeric Δα channels during purification. This construct provided a homogeneous and highly-expressing population. However, the inherent pseudosymmetry from common secondary and tertiary structures between the α, β, and γ subunits of human ENaC hindered particle alignment (*Figure 1d*).

To evaluate biochemical integrity and to facilitate cryo-EM three-dimensional reconstruction of ΔENaC, we generated subunit-specific monoclonal antibodies (mAbs) that bind to three-dimensional epitopes in ΔENaC and FL-ENaC. For immunization, we exploited the high-expressing chicken ASIC (cASIC) by adding the first 22 N-terminal amino acids of cASIC to Δβ, which tolerated the fusion. This construct is referred to hereafter as Δβ$_{ASIC}$. Together, Δα, Δβ$_{ASIC}$, and Δγ comprise ΔENaC$_{ASIC}$ (*Figure 1—figure supplement 3a,b*) (*Jasti et al., 2007*). Two fragment-antigen binding domains (Fabs) were isolated that recognize different epitopes (7B1 and 10D4). While these antibodies were raised against ΔENaC$_{ASIC}$ (*Figure 1—figure supplement 3a,b*), both Fabs bind to both ΔENaC

expressed in HEK 293S GnTI⁻ and FL-ENaC expressed in HEK293T/17, which indicates that ΔENaC is properly folded and that the Fabs do not bind to the ASIC segment (*Figure 1—figure supplement 3c,d*; *Figure 1—figure supplement 4a,b*). Inclusion of 7B1 and 10D4 allowed for proper alignment of the particles (*Figure 1e*). Moreover, maps of the particles with only 10D4 (monoFab) compared to those with both 10D4 and 7B1 (diFab) show that each Fab recognizes only one subunit (*Figure 1—figure supplement 4c–f*). We monitored and compared grid conditions and the resulting data quality (including ice thickness, sample quality, particle distribution, and orientation) between the mono-Fab and the diFab complexes of ENaC and discovered that the diFab complex was a more promising complex for cryo-EM analysis.

Functional characterization of ΔENaC

We investigated ΔENaC function by two-electrode voltage-clamp electrophysiology (TEVC) and whole-cell patch clamp electrophysiology in oocytes and GnTI⁻ HEK cells, respectively (*Figure 2*, *Figure 2—figure supplements 1* and *2a and b*). Unlike FL-ENaC (*Figure 2a*, *Figure 2—figure supplement 2a*), ΔENaC does not exhibit amiloride-sensitive currents in oocytes and HEK cells, and the only Na⁺-specific currents resemble those from uninjected oocytes (*Figure 2—figure supplement 1a,b*). Similarly, oocytes expressing ENaC channels with restored protease sites in the Δ subunits (Δα* and Δγ*) to form Δ*ENaC did not present amiloride-sensitive currents (*Figure 2—figure supplement 1c*). Because HEK cells are better suited to defining whether ΔENaC traffics to the plasma membrane, we examined surface expression of ΔENaC and FL-ENaC expressed in GnTI⁻ HEK cells using confocal microscopy. To ensure robust expression, we transduced the HEK cells with baculovirus encoding the ΔENaC and FL-ENaC proteins, taking advantage of the N-terminal eGFP in the Δγ subunit and the N-terminal eGFP in all three FL subunits to visualize expression, respectively. Based on eGFP fluorescence, we observed robust expression of both ΔENaC and FL-ENaC (*Figure 2—figure supplement 2c,d*). We employed tetramethylrhodamine (TRITC)-labeled 10D4 mAb, an antibody that binds to the extracellular domain of ENaC, to probe the plasma membrane localization of ENaC channels. Indeed, we observed overlapping signals from both eGFP and TRITC-10D4 mAb in cells expressing FL-ENaC but not in cells expressing ΔENaC. Based on the confocal imaging results, ΔENaC is not trafficked to the plasma membrane, in agreement with the electrophysiology results in HEK 293S GnTI⁻ cells and oocytes (*Figure 2—figure supplement 2*).

We further examined whether disruption of the channel by mutagenesis also caused the absence of ΔENaC current. We tested channels comprising a single Δ or Δ* subunit in complex with the two complementary FL-ENaC subunits. Channels comprising Δα-FLβ-FLγ conduct amiloride-sensitive Na⁺ currents which increase approximately 5-fold upon trypsin treatment (compared with 2.2-fold for FL-ENaC, *Figure 2b*, *Figure 2—figure supplements 2* and *3*, and *Figure 2—source data 1*). Since this trypsin response could be a result of cleavage of FLγ, we also tested channels of Δα*-FLβ-FLγ (*Figure 2c*). These channels show an increase in total current compared to Δα-FLβ-FLγ, and demonstrate a more archetypal ENaC current trace (*Figure 2a*, *Figure 2—figure supplement 3*, *Figure 2—source data 1*). These results, in addition to the cleavage pattern of an anti-α immunoblot (*Figure 2—figure supplement 4*) indicate that Δα adopts a biologically relevant fold, capable of forming active channels with other full-length subunits, and that it is likely cleaved once at its N-terminal furin site (RSRA in Δα) but not the C-terminal furin site (AAAA in Δα, *Figure 1—figure supplement 1*). By restoring the protease sites, as in Δα*, the inhibitory peptide was effectively removed.

The FLα-Δβ-FLγ channels conducted amiloride-sensitive Na⁺ currents with a post-trypsin/pre-trypsin ratio of 1.5 (*Figure 2d*, *Figure 2—figure supplement 3*, *Figure 2—source data 1*), similar to that of FL-ENaC. Moreover, an anti-β immunoblot shows no cleavage of Δβ, as expected (*Figure 2—figure supplement 5*).The FLα-FLβ-Δγ channel also conduct an amiloride-sensitive Na⁺ current with approximately 9.5-fold increase upon trypsin treatment (*Figure 2e*, *Figure 2—figure supplements 2* and *3*, and *Figure 2—source data 1*). Although the Δγ subunit has the canonical furin and prostasin sites mutated (AAAA and QQQQ respectively, *Figure 1—figure supplement 1*), there are other basic residues near the furin and prostasin sites that could be cleaved by trypsin. This hypothesis is further supported by the immunoblot showing significant trypsin digestion in Δγ (*Figure 2—figure supplement 6*) as well as the even higher trypsin activation of FLα-FLβ-Δγ* (approximately 13.3-fold, *Figure 2f* and *Figure 2—figure supplement 3* and *Figure 2—source data 1*). Nevertheless, the results are a promising direction for future studies. Importantly, the combination of TEVC traces of
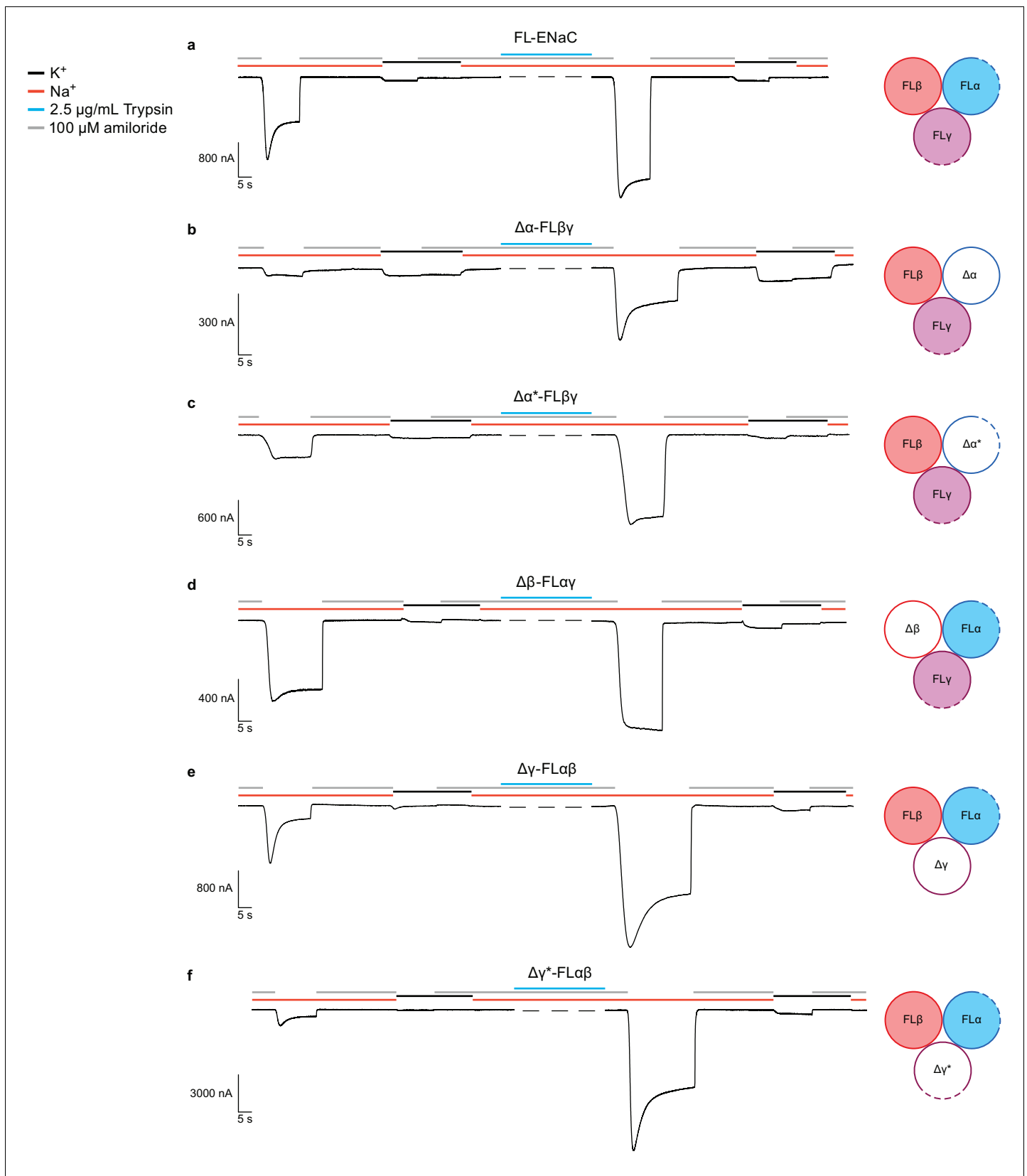
Figure 2. Functional characterization of ΔENaC by TEVC. (**a**) Representative current trace of FL-ENaC shows selectivity of Na$^+$ over K$^+$, block by amiloride and sensitivity to trypsin treatment (2.5 μg/mL for 5 min) by a 2.22 ± 0.49 fold increase in steady state currents post-trypsin treatment (n = 3).

Figure 2 continued on next page

Figure 2 continued

The cartoon located on the right side of each current trace represents the combination of subunits injected in the oocytes. Filled circles represent FL-ENaC subunits while open represent the ΔENaC subunits. Dotted lines represent ENaC subunits that contain the intact protease sites. (b–f) Representative current traces of Δα-FLβγ (b), Δα*-FLβγ (c), Δβ-FLαγ (d), Δγ-FLαβ (e) and Δγ*-FLαβ (f) demonstrate that the ΔENaC subunits can form a functional channel with two FL-ENaC subunits that are selective for Na^+ over K^+ and sensitive to amiloride and trypsin treatment. Currents after trypsin treament increased by 5.15 ± 1.13 (b), 4.42 ± 0.61 (c), 1.46 ± 0.1 (d), 9.52 ± 2.88 (e) and 13.26 ± 5.67 (f) fold (n = 3 for all combinations).
DOI: https://doi.org/10.7554/eLife.39340.008

The following source data and figure supplements are available for figure 2:

Source data 1. Ratio of measured steady state currents pre- and post trypsin treatment.
DOI: https://doi.org/10.7554/eLife.39340.015
Figure supplement 1. Currents measured in oocytes injected with ΔENaC resembles currents observed in uninjected oocytes.
DOI: https://doi.org/10.7554/eLife.39340.009
Figure supplement 2. FL-ENaC and ΔENaC trafficking in HEK 293S GnTI⁻ cells.
DOI: https://doi.org/10.7554/eLife.39340.010
Figure supplement 3. Functional characterization of ΔENaC by TEVC.
DOI: https://doi.org/10.7554/eLife.39340.011
Figure supplement 4. Cleavage of ENaC Δα and FL-α by trypsin shows expected banding.
DOI: https://doi.org/10.7554/eLife.39340.012
Figure supplement 5. Cleavage of ENaC Δβ and FL-β by trypsin shows expected banding.
DOI: https://doi.org/10.7554/eLife.39340.013
Figure supplement 6. Cleavage of ENaC Δγ and FL-γ by trypsin shows expected bands.
DOI: https://doi.org/10.7554/eLife.39340.014

each Δ subunit and the α and γ Δ* counterparts supports ΔENaC representing a biologically relevant channel.

Cryo-EM analysis of ΔENaC

We solved the structure of ΔENaC diFab complex in n-Dodecyl β-D-maltoside (DDM) by cryoEM (*Figure 3*, *Figure 3—source data 1*). We first carried out cycles of 2D and 3D classifications to remove ice contamination, micelles, and denatured complexes. The remaining particles were subjected to unsupervised ab initio 3D classification and refinement in cryoSPARC (*Punjani et al., 2017*) as well as 3D classification and refinement in cisTEM (*Grant et al., 2018*) to arrive at the cryo-EM potential map with a nominal resolution of 4.2 Å from both programs, based on the gold standard FSC = 0.143 and solvent adjusted FSC = 0.143 criteria, respectively (*Figure 3—figure supplement 1*). Additionally, we conducted a masked refinement excluding the flexible Fc domains of the Fabs and micelle in cisTEM (*Figure 3a*), and obtained a map at 3.9 Å, as determined by the solvent adjusted FSC = 0.143 criterion (*Figure 3b,c*), with local resolution estimates generated by BSoft (*Heymann and Belnap, 2007*) indicating regions of the map with a resolution of 3.7 Å (*Figure 3d*).

Discussion

ENaC structural overview

The cryo-EM potential map has three major regions into which the two Fabs and homology models of ΔENaC were manually fitted (*Figure 4*). Alignment of predicted glycosylation sites and aromatic residues to distinct features in the map allowed for the correct assignment of the homology models of the ENaC ECD, generated from the desensitized state of ASIC (PDB: 2QTS, *Figure 4—figure supplements 1–5*, *Figure 4—video 1*). The β subunit is predicted to have 11 glycosylation sites by primary sequence, considerably more than α or γ. Six prominent glycosylation sites were used to assign β (as opposed to the three each in α and γ), whereas a glycosylation on the β9-α4 loop distinguished α from γ (*Figure 1—figure supplement 2*, *Figure 4—figure supplement 1*). Guided by these features and the 10D4 monoFab ΔENaC map, we assigned the identity of 7B1 and 10D4 as binding α and β subunits, respectively (*Figure 4*, *Figure 1—figure supplement 4*).

Forming a trimeric ensemble, the α-β-γ subunits arrange in a counterclockwise manner, as reported by previous studies (*Collier and Snyder, 2011*; *Collier et al., 2014*; *Chen et al., 2011*) (*Figure 4b,d*). The overall domain organization within each subunit of ΔENaC concurs with that of
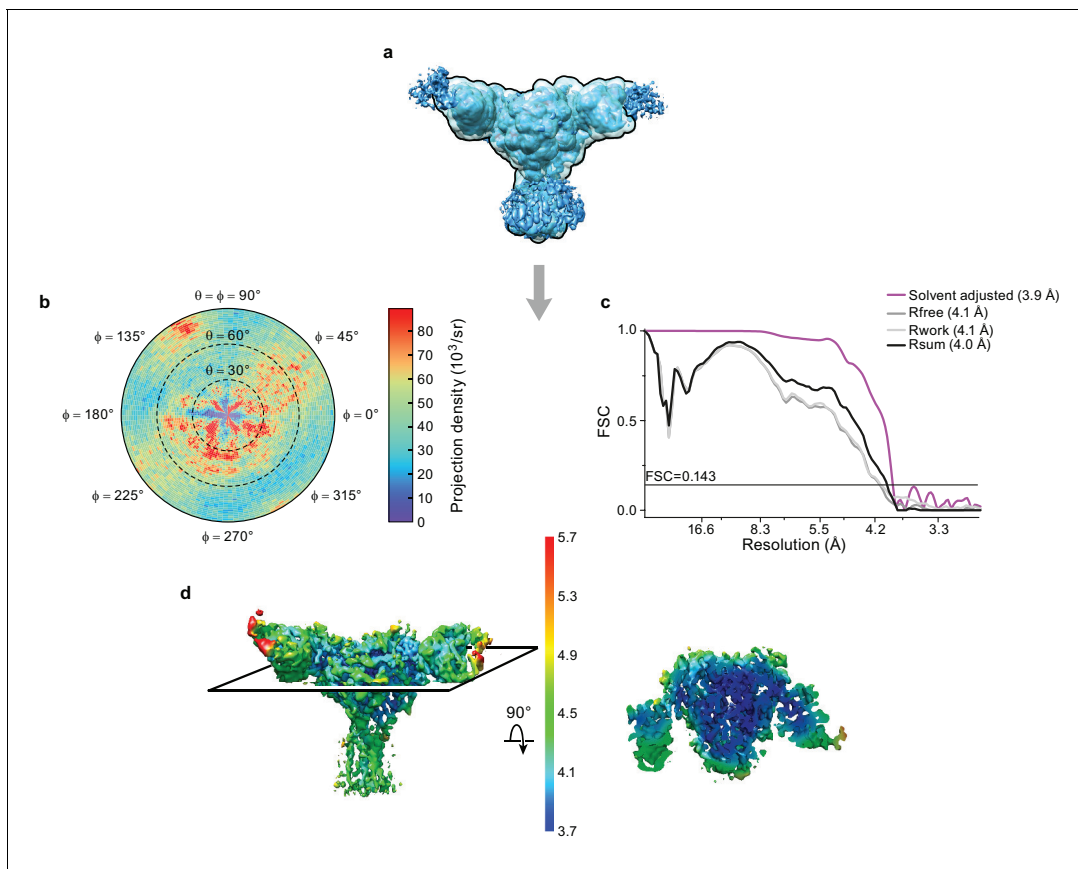
Figure 3. Cryo-EM analysis of final 3D reconstruction map. (**a**) Outline of mask used in the final 3D refinement of ΔENaC-7B1/10D4 complex. (**b**) Angular distribution of particle projections of the ΔENaC-7B1/10D4 complex. (**c**) Solvent adjusted FSC curve (purple) by cisTEM along with FSC curve between the atomic model of ΔENaC-7B1/10D4 complex and half map 1 (R_free – dark grey), half map 2 (R_work – light grey) and final reconstruction map (R_sum – black). The solid line indicates FSC = 0.143. (**d**) 3D map colored according to local resolution estimation using Bsoft. Blue indicates regions where local resolution is estimated to be ~ 3.7 Å.

DOI: https://doi.org/10.7554/eLife.39340.016

The following source data and figure supplement are available for figure 3:

**Source data 1.** Statistics of data collection, three-dimensional reconstruction and model refinement

DOI: https://doi.org/10.7554/eLife.39340.018

Figure supplement 1. Cryo-EM data processing.

DOI: https://doi.org/10.7554/eLife.39340.017

ASIC, which was first illustrated in the crystal structure of chicken ASIC (cASIC) (*Jasti et al., 2007*) (chicken ASIC shares 18 – 20% sequence identity with human ENaC; *Figure 5*, *Figure 5—figure supplement 1*). Each subunit of ΔENaC harbors a cysteine-rich ECD resembling a hand with the palm, knuckle, finger, and thumb domains clenching a 'ball' of β strands. This compact organization is stabilized by eight disulfide bridges in the ECDs of α and γ and nine in β. Seven of the disulfide bonds are conserved throughout the ENaC/DEG family (*Figure 1—figure supplement 1*, *Figure 1—figure supplement 2*, *Figure 5a–c*). The eighth is unique to the three ENaC subunits. For the purpose of consistency in the following discussion, domain and secondary structure assignment in ENaC follow those of ASIC (*Figure 5d*).

At the center of the trimeric architecture of the ECD are β-sheets formed by β1, β3, β6, and β9-β12 that constitute the palm domain, which are divided into two sections, the upper and lower palm domains. The upper palm domain cradles the β-ball, which is composed of β2, β4, β5, β7, and β8 in all three subunits, contrary to previous findings which suggested that the α subunit lacked the β4 and β5 strands (*Stockand et al., 2008*). Completing the 'clench' around the β-ball are the α1 – 3 of the finger, α4 – 5 of the thumb, and α6 of the knuckle domains. The lower palm is directly linked to
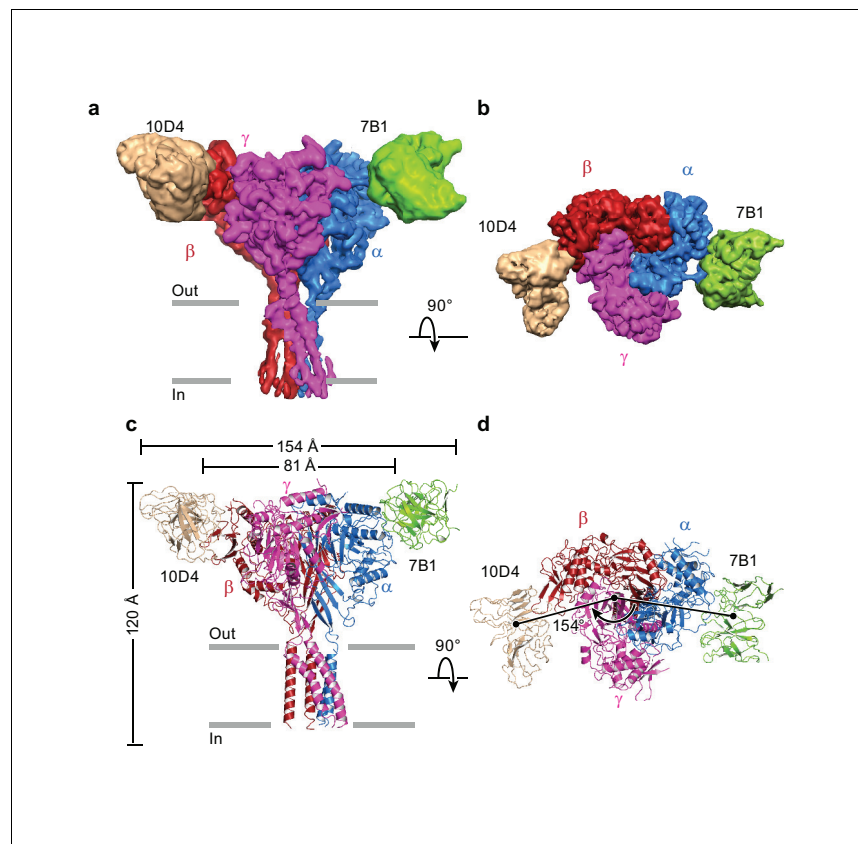
Figure 4. Architecture of the human epithelial sodium channel. (**a**) and (**b**), Cryo-EM map of the ΔENaC-7B1/10D4 complex viewed parallel (**a**) and perpendicular (**b**) to the membrane. The α, β, and γ subunits are colored blue, red, and magenta, respectively. The 7B1 and 10D4 Fv densities are colored green and wheat, respectively. (**c**) and (**d**), Cartoon representation of the ΔENaC-7B1/10D4 complex viewed and colored as in (**a**) and (**b**). The dimensions of the complex and ΔENaC alone are indicated. The centers of mass of the Fv's make 154° angle.

DOI: https://doi.org/10.7554/eLife.39340.019

The following video and figure supplements are available for figure 4:

Figure supplement 1. Unique map features facilitated subunit identification and model building.

DOI: https://doi.org/10.7554/eLife.39340.020

Figure supplement 2. Regions of the Δα ENaC subunit model shown in stick representation superimposed with the potential map in light grey mesh, contoured between 7.5 and 8.0 σ.

DOI: https://doi.org/10.7554/eLife.39340.021

Figure supplement 3. Regions of the Δβ ENaC subunit model shown in stick representation superimposed with the potential map in light grey mesh, contoured between 7.5 and 8.0 σ.

DOI: https://doi.org/10.7554/eLife.39340.022

Figure supplement 4. Regions of the Δγ ENaC subunit model shown in stick representation superimposed with the potential map in light grey mesh, contoured between 7.5 and 8.0 σ.

DOI: https://doi.org/10.7554/eLife.39340.023

Figure supplement 5. Select regions of the GRIP domain in all three subunits.

DOI: https://doi.org/10.7554/eLife.39340.024

Figure 4—video 1. Three dimensional architecture of the ENaC subunits.

DOI: https://doi.org/10.7554/eLife.39340.025

the transmembrane domain (TMD) via β1 and β12 and to the α4 and α5 of the thumb through β9 and β10. The thumb and the lower palm converge to forge interactions with the TMD at a juncture called the 'wrist' (**Figure 5—figure supplement 1**). Underscoring the importance of the wrist region and the critical roles that disulfide bridges play in maintaining the structural and functional integrity of ENaC, alterations of a conserved cysteine, α-Cys479 to an Arg, causes Liddle syndrome due to a missense mutation that not only eliminates a disulfide bridge located at the juncture of the thumb
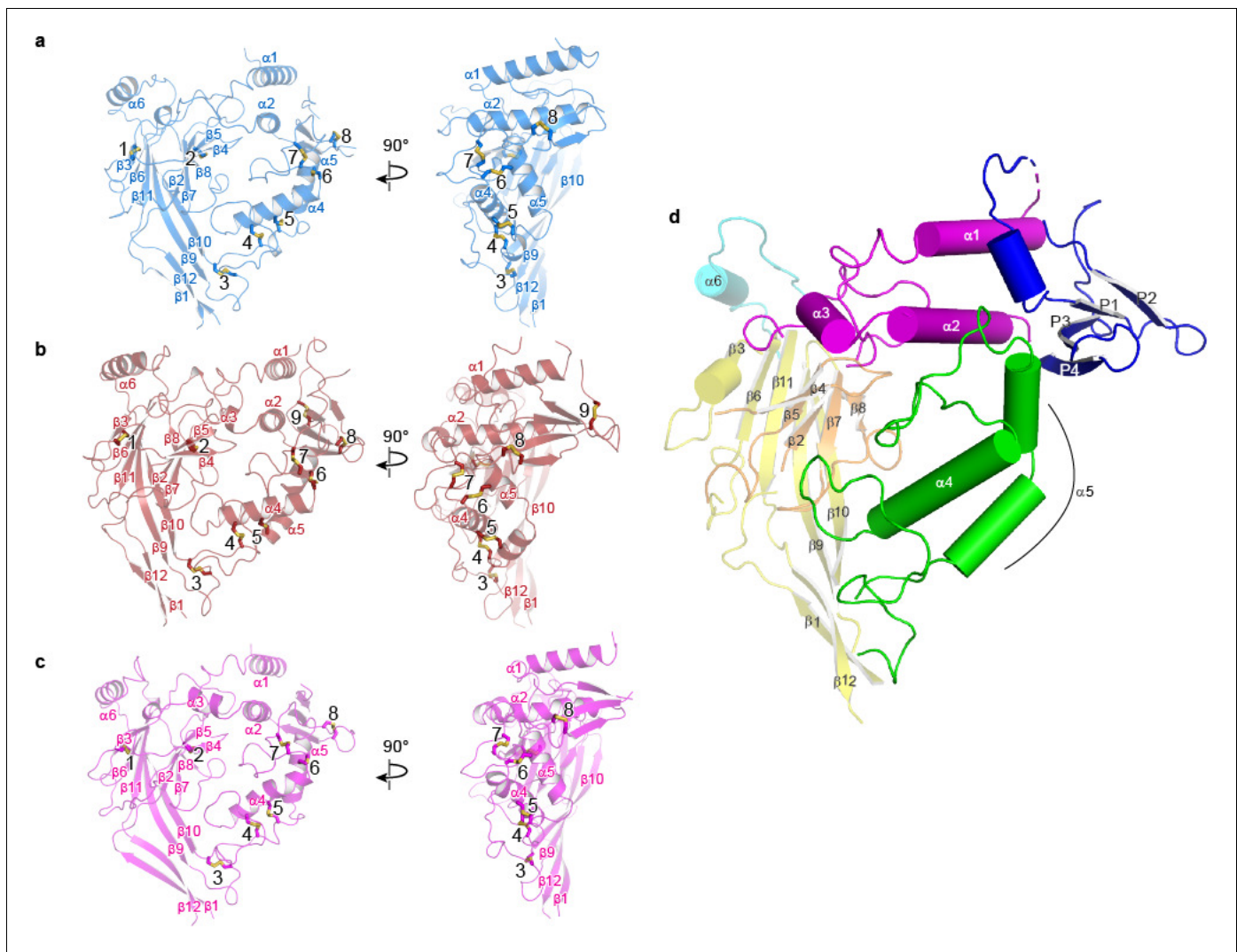
Figure 5. Domain organization in each subunit of ΔENaC resembles a hand clenching a ball. (**a–c**) Domain organization of each ENaC subunit and locations of disulfide bridges. Disulfide bridges 1–7 are conserved across ENaC/DEG family while the eighth disulfide bridge is shared by α (**a**), β (**b**), and γ (**c**) and located in the GRIP domain (P1 - P4). The β subunit contains a ninth disulfide bridge that is also located in the GRIP domain. All subunits are in cartoon representation and colored as in *Figure 4* and the disulfide bridges are in sticks representation. (**d**) Schematic diagram of secondary structure elements of ENaC subunits colored as follows: knuckle, cyan; palm, yellow; finger, purple; GRIP, blue; β-ball, orange; thumb, green.

DOI: https://doi.org/10.7554/eLife.39340.026

The following figure supplement is available for figure 5:

Figure supplement 1. Comparison between ENaC and ASIC subunit structure.

DOI: https://doi.org/10.7554/eLife.39340.027

and palm domains but also introduces a bulky, positively charged residue (*Salih et al., 2017*) (*Figure 5a*).

ENaC differs significantly from ASIC in both structure and primary sequence at the knuckle and finger domains (*Figure 1—figure supplement 1*, *Figure 1—figure supplement 2*, *Figure 5—figure supplement 1*). Each knuckle domain in ENaC makes extensive interactions with the α1 and α2 helices of the finger domain in the adjacent subunit (*Figure 6*). Together, the knuckle and finger domains of all three subunits form a 'collar' at the top of the ECD. Sequence alignment of the three subunits demonstrate divergence in amino acid sequence at the C-terminal end of both α1 and α6 in all three subunits, which results in distinct types of molecular interactions at each subunit interface that are, perhaps, associated with assembly and stability of the ENaC. The contact between the

finger and thumb domains is mediated by long antiparallel helices α1 and α2, which form a barrier between the thumb domain and the β6-β7 loop with α2 making the primary contacts with the thumb domain (*Figure 5—figure supplement 1*, *Figure 6*). The domain arrangement observed in the ΔENaC structure agrees with the functional study probing Na$^+$ binding sites in the α subunit of ENaC (*Kashlan et al., 2015*). The α2 helix makes an almost 90° turn towards the palm domain breaking the helix. This architecture marks another departure from ASIC, in which contacts between the finger and thumb domains are largely mediated by α1, α3, α5, and the α4-α5 loop (*Figure 5—figure supplement 1*).

The TMD is not well ordered, hampering our ability to model the entire TMD region and assign a functional state of the channel. Nevertheless, the EM map offers a glimpse of the positions of TM1 and TM2 on the extracellular side from each subunit (*Figure 6—figure supplement 1*). The overall configuration of the TMD shows that TM2 of all three subunits are positioned near the central axis, poised to mediate ion conduction in agreement with the crystal structures of ASIC and previous elegant functional studies probing ion selectivity and channel block (*Kellenberger and Schild, 2002*). Strikingly, the potential map for γ-TM1 on the extracellular side illustrates clear map for the main chain preceding the β1 strand validating a sequence disparity between the γ subunit and the other ENaC and ASIC subunits (*Figure 6—figure supplement 1*). The γ subunit lacks two residues preceding the palm domain (*Figure 6—figure supplement 1f*). Consequently, interactions within the wrist region in the γ subunit may differ from that of α and β subunits.

The GRIP domain

Previous studies of ENaC have probed stretches of amino acids and their roles in ENaC function by perturbing known protease sites, observing changes in molecular weight, recording channel activity, and conducting cross-linking studies (*Bruns et al., 2007*; *Carattino et al., 2006*). The structure of ΔENaC indicates that these stretches of 20 – 40 amino acids are pieces of larger domains located in the periphery of the ECD near subunit interfaces (*Figure 7*). These stretches of amino acids, located between α1 and α2 are unique to ENaC and are responsible for channel Gating Relief of Inhibition by Proteolysis and will hereafter be referred to as the GRIP domain. Each GRIP domain is composed of a core of β strands that forge interactions with the finger and thumb domains forming a β-sheet 'blanket' that conceals the α2 helix of the finger (*Figure 7—figure supplement 1*). Surprisingly, although the β subunit is not known to gate the channel via proteolysis, it also possesses a GRIP domain with similar organization to those of the α and γ subunits.
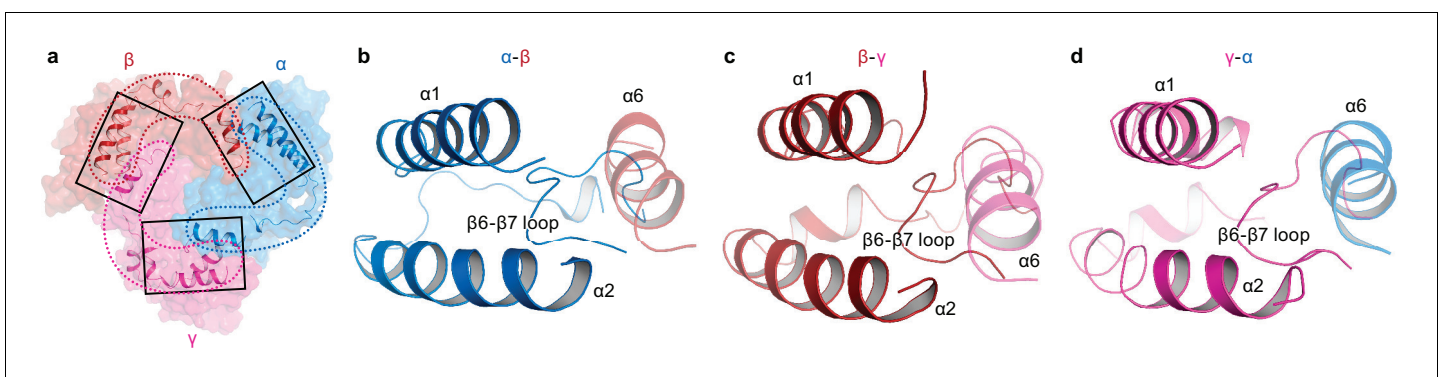

Figure 6. Intersubunit interactions in ΔENaC in the finger and knuckle domains. (a) The finger and knuckle domains forge intersubunit interactions forming a 'collar' at the top of the ECD. Surface representation of ΔENaC viewed perpendicular to the membrane. Subunits are colored as in *Figure 4*. The finger (α1 – 3) and knuckle domains (α6) are shown in cartoon representation. (b–d), Detailed view of the interfaces boxed in (a). The views are parallel to the membrane and show how the helices from the finger and knuckle domains constitute an enclosure around the β6-β7 loop.
DOI: https://doi.org/10.7554/eLife.39340.028

The following figure supplement is available for figure 6:

Figure supplement 1. The ΔENaC structure demonstrates asymmetric interactions at the wrist region.
DOI: https://doi.org/10.7554/eLife.39340.029
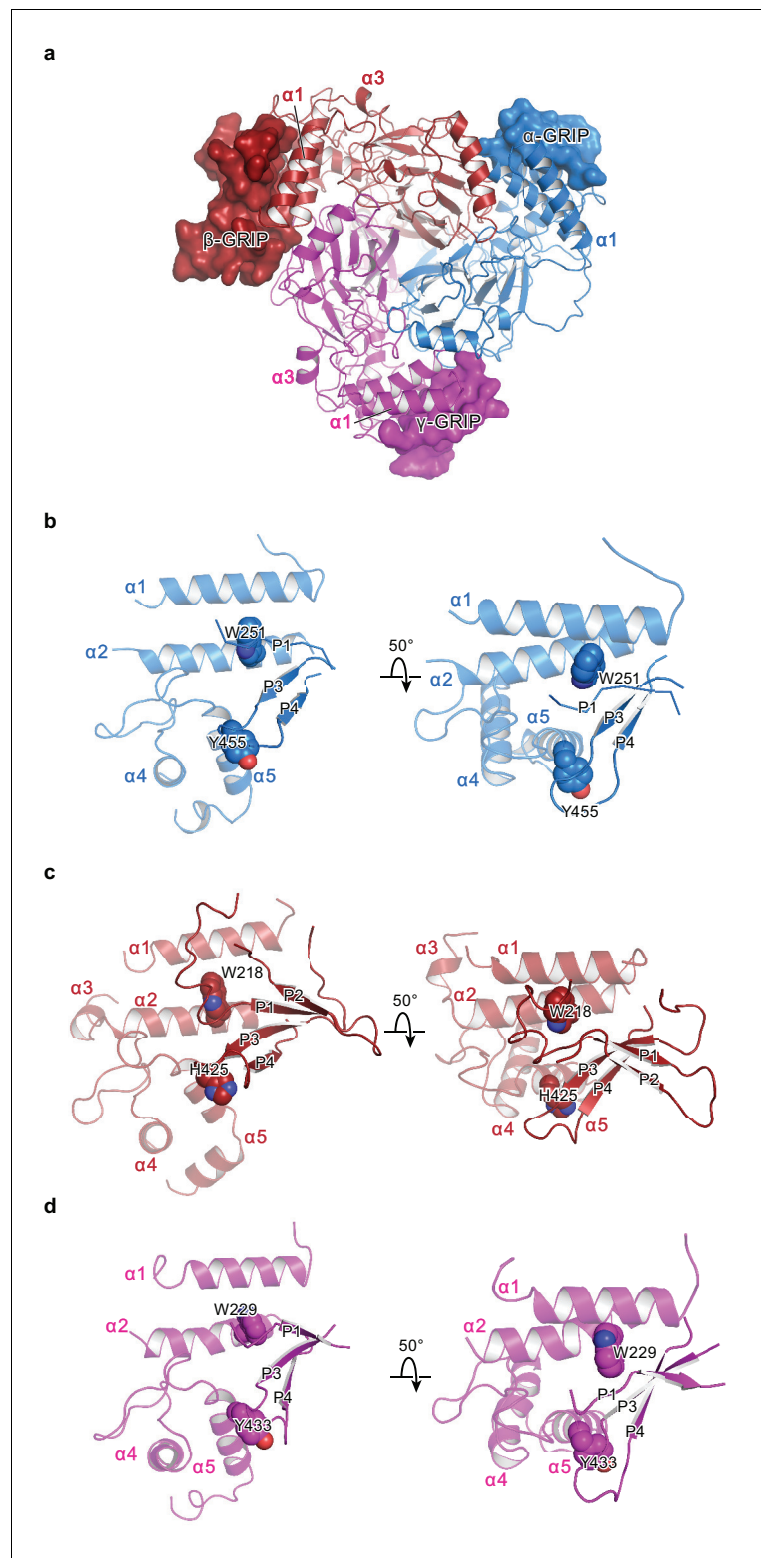
Figure 7. The protease-sensitive domain in ENaC is part of the GRIP domain. (a) ΔENaC is shown in cartoon representation and colored as in *Figure 4*. The GRIP domain is shown in surface representation. Close-up view of the cleft formed by the finger and thumb domains and the P3-P4 segments in α (b), β (c), and γ (d). The cleft is occupied by the P1 segment of the GRIP domain. All three subunits contain conserved tryptophans in α2 (αTrp251, βTrp218, and γTrp229), which interacts with the P1 segment. The P3 and P4 strands are stabilized by the α5 of the thumb domain by docking on top of aromatic residues (αTyr455, βHis425, and γTyr433).

Figure 7 continued on next page

Figure 7 continued

The following figure supplement is available for figure 7:

Figure supplement 1. Cryo-EM map of the P1 segments in α, β, and γ demonstrates critical interactions with the finger and thumb domains.

In all three subunits, the GRIP domains comprise two antiparallel β strands stapled together by a disulfide bond located in the loop that rests against the thumb domain (*Figure 7b–d*, *Figure 7—figure supplement 1b–d*). Furthermore, an additional disulfide bond in the loop near the β-γ interface stabilizes the GRIP domain of the β subunit. We suspect that this additional disulfide bond contributes to the well-ordered behavior of the β GRIP domain, allowing the resolution of nearly the whole segment between α1 and α2 in the β subunit. Moreover, the 10D4 Fab binds the β GRIP domain, allowing us to resolve two additional antiparallel β strands. In the α and γ subunits, we can only identify one stretch of residues that adopt an extended conformation. Based on the shared features observed in all three subunits, it is plausible that the α and γ subunits also contain a fourth β strand. With four possible β strands in the GRIP domains, each strand or stretch of peptides is referred to here as P1-4 (*Figure 7*).

Structural insight gleaned from the β GRIP domain reveals the possible positions of the functionally well-characterized but structurally elusive inhibitory tracts and furin and other protease sites in the α and γ GRIP domains. Studies by the Kleyman group have identified 8- and 11-mer peptide tracts within the α and γ GRIP domains, respectively, which are implicated in channel gating (*Passero et al., 2010*; *Carattino et al., 2008b*; *Kashlan et al., 2010*). Sequence comparison between the three subunits suggests that the inhibitory tracts contain the P1 strand (*Figure 7b – d*, *Figure 7—figure supplement 1b–d*, *Figure 1—figure supplement 1*). Based on this configuration, the first furin site lies at the N-terminal side of P1 whereas the second protease site (furin for α and other protease sites for γ) is likely located at the C-terminal side of P2. The anti-parallel organization of P1 and P2 strands places the two protease sites in close proximity to each other. We speculate that this arrangement allows for efficient proteolysis, especially for the cleavage of the α subunit by furin.
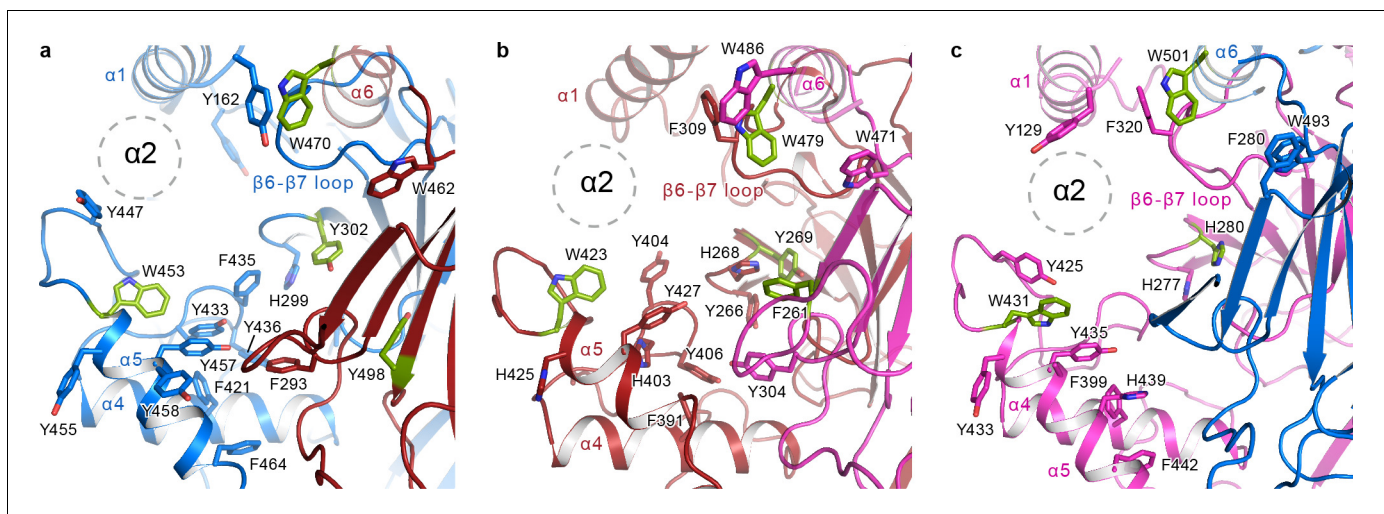
Figure 8. The α2 helix is buried in the aromatic pocket formed by key gating domains in ENaC. The aromatic pockets at the α-β (a), β-γ (b), and γ-α (c) interfaces are shown in cartoon representation. The aromatic residues are shown in sticks representation. Residues conserved in ASIC are colored green. The α2 helices and the GRIP domains are omitted for clarity. The position of the α2 is shown as dotted circles.
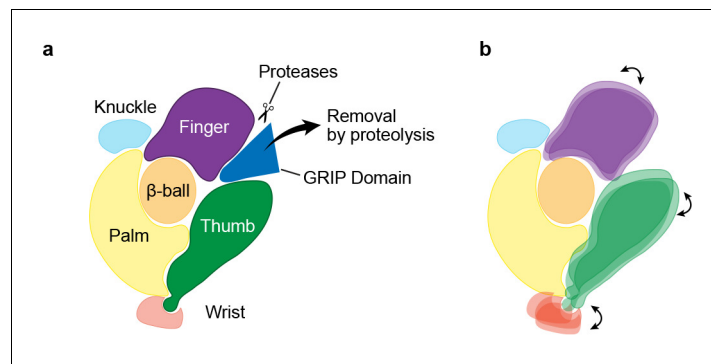
Figure 9. Mechanism of protease-dependent gating in a single ENaC subunit. Removal of the protease sensitive segments of the GRIP domain (**a**) induces conformational changes in the finger and thumb domains (**b**), which is perhaps coupled to ion channel gating through the wrist.

DOI: https://doi.org/10.7554/eLife.39340.033

Aromatic pocket

The first crystal structure of ASIC identified the finger and the thumb domains as major players in ion channel gating. Rearrangements of these domains are coupled to the TMD via the wrist. Additionally, the crystal structure provided insight into the domain essential for fine-tuning ASIC pH-response, deemed the acidic pocket, formed by the β-ball, finger, and thumb domains of one subunit, and the palm domain of the adjacent subunit (*Vullo et al., 2017*). While the acidic pockets in ASIC are lined with negatively charged residues, the equivalent crevices in ENaC are replete with aromatic residues. In fact, aside from Ser428 of Δβ (Asp346 in ASIC), the equivalent sites in the thumb domain that are acidic in ASIC are occupied by tyrosines in all three subunits (*Figure 8*, *Figure 1—figure supplement 1*, *Figure 1—figure supplement 2*) (*Jasti et al., 2007*). Accordingly, the pocket that is largely occupied by α2 in ΔENaC is referred to here as the aromatic pocket.

Tucked in the aromatic pocket, α2 makes contacts with all critical elements of the gating machinery in ENaC. This observation is consistent with studies finding that site-directed mutagenesis perturbing residues in the α2 results in changes in Na^+ self-inhibition and binding of the P1 segment of the GRIP domain (*Kashlan et al., 2010*). In all three ENaC subunits, the α2 forms contacts with the thumb, α1 helix, the β6-β7 loop and the GRIP domain, and with the knuckle and the upper palm domains in the adjacent subunit (*Figure 8*). Moreover, studies using synthesized 8-mer (LPHPLQRL) and 11-mer peptides (RFLNLIPLLVF) (*Passero et al., 2010*), the inhibitory peptides of α and γ subunits, respectively, have identified residues in α2 to be critical to the binding of the inhibitory peptides. These peptides pack against α2 and form a wedge between the thumb domain and α1 in the ΔENaC structure (*Figure 7b–d* and *Figure 7—figure supplement 1b–d*). These inhibitory peptides contain prolines that introduce a kink within the tract that may serve as a point that divides P1 into two segments: the N-terminal side, which interacts with the finger and thumb; and the C-terminal side, which interacts primarily with α2 and P3. The observed orientation of the P1 segment is consistent with the cross-linking experiments by Kashlan et al., which provided two major findings: (1) the inhibitory tracts adopt an extended conformation and (2) the N-terminal side of the peptide binds near the thumb/finger interface (*Kashlan et al., 2010*; *Kashlan et al., 2012*).

The potential map for α-P1 suggests that the N-terminal side mirrors that of β-P1 forging contacts with the α1 helix (*Figure 7—figure supplement 1b,c*). In contrast, the potential map for the γ-P1 suggests that the peptide interacts with the thumb and α1/α2 more extensively and extends toward α3 (*Figure 7—figure supplement 1d*). These distinct points of contact with the finger and thumb domains between the α- and γ-P1 segments may influence the extent to which the subunits influence channel P_o. While removal of the inhibitory tract in α transitions the channel to an intermediate P_o state, excision of the γ-P1 segment places the channel in the high P_o state; this high P_o state can be accomplished without the removal of the α-P1 (*Carattino et al., 2008a*). The visual evidence of direct interactions between P1 and the finger and thumb domains demonstrated in the ΔENaC structure sheds light into how these inhibitory tracts can modulate channel function in ENaC.

Mechanism

ΔENaC follows a common organization that was first observed in ASICs: a scaffolding structure in the upper palm, the flexible lower palm which is tethered to the TM and thumb, and the β-ball (*Figure 5—figure supplement 1*) (*Jasti et al., 2007*). However, the specialized finger domains deviate from what is observed in ASIC and such deviations accommodate the distinct functions between the proton sensors of ASIC and the protease-sensitive regulators of ENaC.

Key gating structures are preserved, albeit with specific structural configurations in both ASIC and ENaC supporting the idea that the superfamily of ENaC/DEG channels conform to a gating scheme that involves conformational changes of the finger and thumb domains, rearrangements that are propagated to the ion channel via the wrist (*Jasti et al., 2007*). In the case for ENaC, a speculative model for gating involves proteolysis and the subsequent removal of the P1 segment, which serves as a wedge, inducing rearrangements of the finger and thumb domains (*Figure 9*).

The structural work presented here provides new insight into ENaC assembly and gating. The structure unveils the positions of the GRIP domains, specifically the key peptidyl tracts that inhibit ENaC activity, and the distinct interactions that they mediate with the finger and thumb domains. Furthermore, it reveals that there are different interactions between the finger and knuckle domains at each subunit interface, and between the base of the thumb and the TMD in the wrist region suggesting that each subunit differentially contributes toward gating the channel, supporting electrophysiological findings. Importantly, the structure provides the first molecular model for protease-dependent regulation of ENaC opening and Na^+ and water homeostasis.

Materials and methods

Key resources table

Reagent type (species) or resource	Designation	Source or reference	Identifiers	Additional information
Gene (*Homo sapiens*)	amiloride-sensitive sodium channel subunit alpha isoform 1	Synthetic	NCBI Reference Sequence: NP_001029.1	Gene sysnthesized by BioBasic
Gene (*Homo sapiens*)	amiloride-sensitive sodium channel subunit beta	Synthetic	NCBI Reference Sequence: NP_000327.2	Gene sysnthesized by BioBasic
Gene (*Homo sapiens*)	amiloride-sensitive sodium channel subunit gamma	Synthetic	NCBI Reference Sequence: NP_001030.2	Gene sysnthesized by BioBasic
Cell line (*Homo sapiens*)	HEK293S GnTI-	ATCC	Cat # ATCC CRL-3022	
Cell line (*Homo sapiens*)	HEK293T/17	ATCC	Cat # ATCC CRL-11268	
Antibody	7B1	OHSU VGTI, Monoclonal Antibody Core	AB_2744525	Isotype IgG2a, kappa
Antibody	10D4	OHSU VGTI, Monoclonal Antibody Core	AB_2744526	Isotype IgG1, kappa
Recombinant DNA reagent	pEG BacMam	Gift from Eric Gouaux	doi: 10.1038/nprot.2014.173	
Commercial assay or kit	mMessage mMachine T7 Ultra Transcription	Ambion	AM1345	
Chemical compound, drug	Amiloride hydroschloride hydrate	Sigma	A7410	
Chemical compound, drug	Phenamil mesylate	Tocris	Cat # 3379	
Software, algorithm	Relion-2.0	doi: 10.1016/j.jsb.2012.09.006	RRID:SCR_016274	https://www2.mrc-lmb.cam.ac.uk/relion/index.php?title=Main_Page

Continued on next page

Continued

Reagent type (species) or resource	Designation	Source or reference	Identifiers	Additional information
Software, algorithm	DoG picker	doi: 10.1016/j.jsb.2009.01.004	OMICS_27772	https://omictools.com/dog-picker-tool
Software, algorithm	MotionCor2	doi:10.1038/nmeth.4193	SCR_016499	http://msg.ucsf.edu/em/software/motioncor2.html
Software, algorithm	Gctf	doi:10.1016/j.jsb.2015.11.003	SCR_016500	https://www.mrc-lmb.cam.ac.uk/kzhang/Gctf/
Software, algorithm	cryoSparc	doi:10.1038/nmeth.4169	SCR_016501	https://cryosparc.com/
Software, algorithm	cisTEM	https://doi.org/10.1038/nmeth.4672	SCR_016502	https://cistem.org/
Software, algorithm	Bsoft	doi:10.1006/jsbi.2001.4339	SCR_016503	https://lsbr.niams.nih.gov/bsoft/
Software, algorithm	Pymol	PyMOL Molecular Graphics System, Schrŝdinger, LLC	RRID:SCR_000305	http://www.pymol.org/
Software, algorithm	UCSF Chimera	doi:10.1002/jcc.20084	RRID:SCR_004097	http://plato.cgl.ucsf.edu/chimera/
Software, algorithm	Coot	https://doi.org/10.1107/S0907444904019158	RRID:SCR_014222	https://www2.mrc-lmb.cam.ac.uk/personal/pemsley/coot/
Software, algorithm	Rosetta	https://doi.org/10.1371/journal.pone.0020450	RRID:SCR_015701	https://www.rosettacommons.org/
Software, algorithm	Phenix	doi:10.1107/S2059798318006551	RRID:SCR_014224	https://www.phenix-online.org/
Software, algorithm	Jpred4	https://doi.org/10.1093/nar/gkn238	SCR_016504	www.compbio.dundee.ac.uk/jpred/
Software, algorithm	Psipred v3.3	https://doi.org/10.1093/bioinformatics/16.4.404	RRID:SCR_010246	www.bioinf.cs.ucl.ac.uk/psipred
Software, algorithm	QUARK	doi:10.1002/prot.24065 (2012)	OMICS_10835	https://omictools.com/quark-tool
Software, algorithm	Molprobity	doi:10.1107/S0907444909042073	RRID:SCR_014226	http://molprobity.biochem.duke.edu

Construct design

The cDNA encoding the full length α, β and γ subunits of human ENaC were cloned into pEG Bac-Mam expression vector harboring an N-terminal eGFP (*Goehring et al., 2014*). The Δα was generated by removing both N- and C-terminal segments and modifying the furin sites obtaining a mutant variant of the α subunit lacking 42 and 89 residues at N- and C- termini, respectively. While the Δβ was designed to possess truncations of 30 and 79 residues at the N- and C-terminal regions, $\Delta\beta_{ASIC}$ has the same truncated regions as Δβ but contains an additional N-terminal 2 – 22 residues of cASIC upstream of Δβ. Lastly, Δγ lacks 20 and 79 residues at the N- and C-terminal domains, has modified furin and prostasin sites, and includes a Strep-tag II, an octa-histidine tag, eGFP, and Thrombin cleavage site at the N-terminus.

Generation and isolation of Fabs

Mouse monoclonal antibodies 7B1 and 10D4 were generated using standard procedure by Dan Cawley at the Vaccine and Gene Therapy Institute (OHSU). Liposomes containing asolectin:cholesterol:lipidA:brain polar lipid extract (BPLE) (16:4.6:1:5.3) were prepared in 20 mM Tris, 150 mM NaCl at pH 8.0 at a concentration of 40 mg/ml. The mixture was subjected to repeated freeze-thaw cycles followed by extrusion through a 200-nm filter. Purified $\Delta ENaC_{ASIC}$ (Δα, $\Delta\beta_{ASIC}$, Δγ) protein was added to the liposome mixture in the presence of 400 mM NaCl and 0.8% Na-cholate and passed through a PD-10 desalting column to remove excess salt and detergent. Mice were immunized with approximately 30 μg of the reconstituted $\Delta ENaC_{ASIC}$ for generation of hybdridoma cell lines

eLIFE Research article

Structural Biology and Molecular Biophysics

(*Figure 1—figure supplement 3*). Monoclonal antibodies were screened by FSEC and BioDot blot to identify clones that recognize tertiary or primary epitopes. The 7B1 and 10D4 mAbs were selected because they recognize tertiary epitopes of ENaC. The mAbs were purified, and their Fabs were generated by papain cleavage. Fab 7B1 was isolated by anion exchange using HiTrap Q HP column while Fab 10D4 was eluted using Protein A column to remove Fc. After isolation, both Fabs were dialyzed in 200 mM NaCl and 20 mM Tris at pH 8.0.

Expression and purification of ΔENaC-Fab complexes

Human embryonic kidney cells lacking N-acetylglucosaminyltransferase I (HEK293S GnTI⁻ cells) were grown in suspension at a density of $2-4 \times 10^6$ cells / ml in Freestyle medium with 2% FBS and transduced with the virus (Δα, Δβ and Δγ) at a multiplicity of infection (MOI) of 1 and incubated at 37°C. Eight hours post-transduction, sodium butyrate and phenamil mesylate were added to 10 mM and 500 nM, respectively, and cells were incubated at 30°C. After 36 hr, the cells were collected by centrifugation at 4790 xg for 15 min. The pellet was washed with 20 mM Tris, 200 mM NaCl and followed by a second round of centrifugation at 4790 xg for 15 min. Cells were homogenized with a dounce homogenizer and sonicated in 20 mM Tris, 200 mM NaCl, 5 mM $MgCl_2$, 25 µg/ml DNase I and protease inhibitors. Lysed cells were centrifuged at 9715 xg for 20 min; the resulting supernatant containing the membrane fraction was further centrifuged at 100,000 xg for 1 hr. Membrane pellets were resuspended and solubilized in 20 mM TRIS pH 8, 200 mM NaCl, 20 mM n-dodecyl-β-D-maltopyranoside (DDM, Anatrace), 3 mM cholesteryl hemisuccinate (CHS), 2 mM ATP, 2 mM $MgSO_4$, protease inhibitor and 25 U/mL nuclease for 1 hr at 4°C. The solubilized fraction was isolated by ultracentrifugation 100,000 xg for 1 hr, and ΔENaC was bound to streptactin resin packed into an XK-16 column. The column was washed with 20 mM TRIS, 200 mM NaCl, 0.5 mM DDM, 75 µM CHS and 25 U/mL nuclease, followed by an additional wash of the same buffer containing 2 mM ATP, and eluted with 2.5 mM desthiobiotin. The eluted fractions were concentrated and then incubated with either one Fab 10D4 (monoFab complex) or two Fabs 7B1 and 10D4 (diFab complex) in a 1:3 molar ratio of ENaC:Fab for 10 min, and clarified by ultracentrifugation 100,000 xg for 1 hr. The supernatant was injected onto a Superose 6 Increase 10/300 GL column equilibrated in 20 mM TRIS pH 8.0, 200 mM NaCl, 0.5 mM DDM, 75 µM CHS and 1 mM TCEP to isolate the protein complex by size-exclusion chromatography. Monodispersed fractions were pooled and concentrated to 2.2 mg/mL.

For FSEC experiments analyzing peak shifts of the ΔENaC and FL-ENaC with 7B1 and 10D4, ΔENaC was expressed in HEK 293S GnTI⁻, as described above, while FL-ENaC was expressed in HEK 293T/17. The HEK 293T/17 cells were grown in suspension at a density of $2-4 \times 10^6$ cells / ml in Freestyle medium with 2% FBS and transduced with the virus (FL-α, FL-β and FL-γ) at a multiplicity of infection (MOI) of 1 and incubated at 37°C. Eight hours post-transduction, 500 nM phenamil mesylate was added, and cells were incubated at 30°C. After 36 hr post-transduction, the cells were collected by centrifugation at 4790 xg for 15 min. The pellet was washed with 20 mM Tris, 200 mM NaCl and followed by a second round of centrifugation at 4790 xg for 15 min. Cell pellets were resuspended and solubilized in 20 mM TRIS pH 8, 200 mM NaCl, 20 mM n-dodecyl-β-D-maltopyranoside (DDM, Anatrace), 3 mM cholesteryl hemisuccinate (CHS), protease inhibitor and 25 U/mL nuclease for 1 hr at 4°C. The solubilized fraction was isolated by ultracentrifugation 100,000 xg for 1 hr, then incubated with either one Fab (7B1 or 10D4) or two Fabs (7B1/10D4) in a 1:3 molar ratio of ENaC:Fab for 10 min, and clarified by ultracentrifugation 100,000 xg for 1 hr. The supernatant was injected onto a Superose 6 Increase 10/300 GL column for FSEC analysis.

Immunoblotting

Aliquots of 7 µg purified ENaC were incubated with 2.5 µg/mL trypsin for 10 min at room temperature. These samples were then run through 4 – 20% Criterion SDS-PAGE gels and blotted onto nitrocellulose membranes according to manufacturer's instructions (Bio-Rad). After blocking overnight in 5% non-fat milk in TBS, membranes were incubated in primary antibody (ENaC α subunit, 6 µg/blot SC-21012; ENaC β subunit, 6 µg/blot SC-21013; ENaC γ subunit, 10 µg/blot abcam ab133430) for 2 hr. The membranes were then incubated in 1 µg/blot IRDye 800CW goat anti-rabbit IgG (Licor) for 1 hr.

Image acquisition and processing

Purified ΔENaC-Fab complexes were applied to glow-discharged Quantifoil holey carbon grids (Au 1.2 μm/1.3 μm hole space/hole separation, 300mesh), blotted using a Vitrobot Mark III (FEI) with the following conditions, 7 s wait time, and 5 s blot time at 100% humidity, and then plunge-frozen in liquid ethane cooled by liquid nitrogen. All images were collected on a Titan Krios electron microscope operating at 300 kV at the Multiscale Microscopy Core (OHSU). Images were recorded by a Gatan K2 Summit direct electron detector operating in super-resolution mode, and the images were collected using the automated acquisition program SerialEM (*Mastronade, 2003*). Magnification of the recorded images corresponded to a pixel size of 1.33 Å in counting mode (0.665 Å in super-resolution mode). For the ΔENaC-10D4 complex, two data sets were acquired and were initially processed separately, and subsequently combined for 3D reconstruction. Each image in the first dataset was dose-fractionated to 30 frames with 0.5 s per frame and a total exposure time and dose of 15 s and 54 e^-/$Å^2$, respectively. The second dataset was collected in counting mode, and was therefore not binned when combined with the first where each image was dose-fractionated to 60 frames with 0.25 s per frame and a total exposure time and dose of 15 s and 50 e^-/$Å^2$, respectively. Similarly, two separate datasets were obtained for ΔENaC-7B1/10D4 complex in super-resolution mode. Like in the monoFab complex, each data set was processed separately and later combined for further analysis and 3D reconstruction. The images of the first dataset of the diFab complex were dose-fractionated to 40 frames with 0.25 s per frame and a total exposure time and dose of 10 s and 62 e^-/$Å^2$, respectively, while the images of the second dataset were dose-fractionated to 48 frames with 0.25 s per frame and a total exposure time and dose of 12 s and 71 e^-/$Å^2$, respectively.

The ΔENaC-10D4 data set collected in super-resolution mode was binned 2 × 2 while the ΔENaC-10D4 data set collected in counting mode was left unbinned. Both data sets were motion corrected using MotionCor2 (*Zheng et al., 2017*), and automated particle selection was performed using DoGPicker (*Voss et al., 2009*). Defocus values for individual particles were estimated using Gctf (*Zhang, 2016*), and particles belonging to low-abundance classes were removed via 2D classification and 3D classification in RELION (*Scheres, 2012*). The final set of particles was further analyzed in cryoSPARC and refined to a nominal resolution of 5.4 Å (*Punjani et al., 2017*).

For the ΔENaC-7B1/10D4 data sets, super-resolution counting images were 2 × 2 binned, and motion corrected using MotionCor2. Manual and automated particle selections were performed where DoGPicker was utilized for the latter resulting in a total of 667,984 particles. Defocus values for individual particles were estimated using Gctf, and particles of low-abundance classes via 2D classification in RELION were removed. For 3D classification in RELION, a reference model of a low-resolution map of ENaC-7B1/10D4 obtained from a data set (14.4 Å) was low-pass filtered to 50 Å, and particles were classified into two classes where the major class contained 385,997 particles. Duplicates (as a result of RELION2.0 re-centering particles after 2D classification) and particles close to micrograph edges were removed, resulting in 329,180 particles that were subjected to *ab initio* 3D classification in cryoSPARC (*Punjani et al., 2017*), and 3D classification and refinement in cisTEM (*Grant et al., 2018*). Particles belonging to the low abundance class in cryoSPARC and cisTEM were discarded yielding 244,223 and 290,007 particles, respectively. Using default settings in cryoSPARC, particles with class probability of > 0.9 were used for refinement; thus, final reconstruction and refinement used 244,223 particles. For cisTEM, initial 3D classification and refinement was done using a refinement threshold of 8 Å and applying a mask during the last few iterations that excluded the constant domain (Fc) of the Fabs. During this process, we noticed that extraneous features, such as the micelle, were having a strong influence on alignment and classification, so the cisTEM particles were then re-processed using a mask that excluded both the micelle and the Fc of the Fabs, and aligned with a 5.4 Å limit. This dataset consisted of 302,263 particles and improved the resolution, as determined by the FSC = 0.143 criterion (~3.9 Å). More importantly, the electrostatic potential map was notably improved in the regions of interest. The resolutions reported in *Figure 3—source data 1* are based on the FSC = 0.143 criterion (gold-standard in the case of RELION and cryoSPARC). Final resolution reported in *Figure 3—source data 1* are solvent adjusted FSC = 0.143 criterion. No symmetry was applied during data processing.

Model building

Homology models of the human α, β, and γ subunits were generated with the crystal structure of cASIC (*Jasti et al., 2007*) (PDB code: 2QTS, chain A) as a template using SWISS-MODEL server and homology models for the Fabs were also generated by SWISS-MODEL (*Arnold et al., 2006*). All models were docked into the EM potential in UCSF Chimera then rigid-body fitted into the EM potential using Coot (*Pettersen et al., 2004*; *Emsley and Cowtan, 2004*). We incorporated models generated from Rosetta (*DiMaio et al., 2011*) into manual fitting and adjustments during model-building in Coot to build the palm, knuckle, TM, thumb, β-ball, and finger domains. To build the GRIP domains, we integrated analysis from Jpred4, PSIPRED v3.3, and QUARK online *ab initio* protein structure prediction to support our analysis of the cryo-EM map (*Buchan et al., 2013*; *Xu and Zhang, 2012*; *Drozdetskiy et al., 2015*). The final model was subjected to refinement using the module phenix.real_space_refine in PHENIX (*Adams et al., 2011*).

The cryo-EM map in all three subunits preceding the N-terminal side of the α2 helices was unambiguous and showed features consisting of two β-strands connected by a loop, the P3 and P4 segments of the GRIP domains (*Figure 4—figure supplement 5*). Secondary structure prediction analysis by online servers Jpred4, PSIPRED v3.3, and QUARK supported this observation (*Buchan et al., 2013*; *Xu and Zhang, 2012*; *Drozdetskiy et al., 2015*). We found that the potential map in the β subunit had the best-defined feature demonstrating four β strands (*Figure 4—figure supplement 5*). Based on the cryo-EM map, the P1 segments in α and γ adopt β strand-like conformations, like in the β subunit, which is also supported by the secondary structure prediction servers (*Figure 4*, *Figure 4—figure supplement 5*). The regions between P1 and P3 in the α and γ subunits, however, are disordered in the cryo-EM map. We built stretches of residues into the P1 potential maps in the α- and γ-GRIP domains using sequence alignment with the β-GRIP domain and cryo-EM potential map features as guides.

For validation, FSC curves were calculated between the final model and the EM map as well as the two half maps generated by cisTEM. We implemented MolProbity to analyze geometries of the atomic model (*Chen et al., 2010*). All figures of map and atomic model were prepared using UCSF Chimera and Pymol (*Pettersen et al., 2004*).

Two-electrode voltage clamp electrophysiology

All constructs used for two-electrode voltage clamp electrophysiology (TEVC) experiments were cloned into pGEM vector, linearized and transcribed to mRNA using mMESSAGE mMACHINE T7 Ultra Kit (Ambion) procedure. *Xenopus laevis* oocytes purchased from Ecocyte were injected with a volume of 50 nL containing either 0.5 – 1.0 ng of each FL-ENaC subunit mRNA or 5 ng of each ΔENaC and Δ*ENaC subunit mRNA. For experiments containing combinations of FL-ENaC and ΔENaC, 5 ng of each subunit mRNA was injected. Oocytes were incubated at 16°C for 12 – 48 hr in the presence of 100 µM amiloride and 250 µg/mL amikacin. The recordings were performed using two different ionic solutions with or without 100 µM amiloride (110 mM KCl and 110 mM NaCl) where all buffers additionally contained 1.8 mM $CaCl_2$ and 10 mM HEPES (pH 7.4). Macroscopic ENaC currents are defined as the difference between inwards currents obtained in the absence and in the presence of 100 µM amiloride. To test full activation of ΔENaC constructs, 2.5 µg/mL Trypsin was perfused for 5 min in the presence of 100 µM amiloride. Amiloride-sensitive currents were recorded prior to Trypsin treatment as well as after in order to determine the increase in current amplitude. All recording experiments were carried out at a holding potential of −60 mV and repeated independently at least three times.

Whole-cell patch clamp electrophysiology

HEK293S GnTI⁻ cells were grown in suspension at a density of $2-4 \times 10^6$/ml in Freestyle medium with 2% FBS and transduced with the virus (Δα, Δβ, and Δγ; or FL-α, FL-β, and FL-γ) at a multiplicity of infection (MOI) of 1 and incubated in the presence of 500 nM phenamil mesylate at 30°C for 12 hr. Five hours before recording, cells were transferred to wells containing glass coverslips at a density of $0.3 - 0.5 \times 10^6$ cells/ml and in Dulbecco's Modified Eagle Medium supplemented with 5% FBS and 500 nM phenamil mesylate. Whole-cell recordings were carried out 17 – 24 hr after transduction. Pipettes were pulled and polished to 2 – 2.5 MΩ resistance and filled with internal solution containing (in mM): 150 KCl, 2 $MgCl_2$, 5 EGTA and 10 HEPES (pH 7.35). External solution contained

(in mM): 150 NaCl, 2 $MgCl_2$, 2 $CaCl_2$, 10 HEPES (pH 7.4), and 0.1 amiloride. Test external solution did not contain 0.1 mM amiloride. As in TEVC experiments, macroscopic ENaC currents are defined as the difference between inwards currents obtained in the absence and in the presence of 100 µM amiloride. Holding potential was at −60 mV.

Confocal microscopy

Six mg of mAb 10D4 was dialyzed into 0.2 M carbonate-bicarbonate (Na_2CO_3/$NaHCO_3$) solution buffered at pH 9.0. The dialyzed mAb was concentrated to 6 mg/mL. Tetramethylrhodamine (TRITC, ThermoFisher 46112) was dissolved in DMSO at a final concentration of 1 mg/mL. To the 10D4 solution, 35 µg of TRITC was slowly added and mixed thoroughly. The 10D4-TRITC mix was incubated at room temperature in the dark for 2 hr followed by gel filtration to remove excess TRITC. The carbonate-bicarbonate buffer was exchanged with Tris-buffered saline buffer (200 mM NaCl, 20 mM TRIS, pH 8.0) using PD-10 desalting column. The dye:protein molar ratio of the final TRITC-labeled mAb 10D4 in TBS buffer was approximately 2.8.

HEK293S GNTI⁻ cells were resuspended from DMEM into 2 mL HBSS media, stained with 10 µg (5 µg/µL stock) of WGA Alexa Fluor 647 conjugate (ThermoFisher W32466) and 170 µg (4.9 µg/µL stock) of 10D4-TRITC and subsequently incubated at 37°C for 10 min. The cells were then washed with PBS two times before resuspended in 1 mL HBSS. Live cell imaging was performed on a Yokogawa CSU-W1 spinning disk confocal microscope using a 60 × 1.4 Plan Apo VC objective. Images were acquired at a pixel size of 0.108 µm for three different wavelengths, starting at 640 nm, 561 nm and then 488 nm. Exposure time varied depending on sample intensity, but remained the same for each wavelength between the two samples of infected cells (FL-ENaC and ΔENaC), 400 ms for 640 nm, 2 s for 561 nm and 600 ms for 488 nm. Images were imported into Fiji for image analysis.

Additional information

Author contributions

Sigrid Noreng, Data curation, Formal analysis, Validation, Investigation, Visualization, Methodology, Writing—original draft, Writing—review and editing, Performed sample preparation, Collected, analyzed, and processed cryo-EM data, Carried out electrophysiology and confocal microscopy experiments; Arpita Bharadwaj, Conceptualization, Formal analysis, Validation, Visualization, Methodology, Writing—original draft, Writing—review and editing, Performed sample preparation and collected cryo-EM data; Richard Posert, Validation, Investigation, Visualization, Methodology, Writing—review and editing, Designed ENaC constructs; Craig Yoshioka, Data curation, Formal analysis, Validation, Investigation, Visualization, Methodology, Writing—original draft, Writing—review and editing, Collected, analyzed, and processed cryo-EM data; Isabelle Baconguis, Conceptualization, Resources, Data curation, Formal analysis, Supervision, Funding acquisition, Validation, Investigation, Visualization, Methodology, Writing—original draft, Project administration, Writing—review and editing,

Carried out preliminary characterization and purification, Performed electrophysiology, model-building and refinement

Author ORCIDs
Sigrid Noreng http://orcid.org/0000-0001-5767-1399
Arpita Bharadwaj http://orcid.org/0000-0002-3867-7610
Richard Posert http://orcid.org/0000-0001-9010-2104
Craig Yoshioka https://orcid.org/0000-0002-0251-7316
Isabelle Baconguis http://orcid.org/0000-0002-5440-2289

Decision letter and Author response
Decision letter https://doi.org/10.7554/eLife.39340.042
Author response https://doi.org/10.7554/eLife.39340.043

Additional files

Supplementary files
• Transparent reporting form
DOI: https://doi.org/10.7554/eLife.39340.034

Data availability
The three-dimensional cryo-EM density map and the coordinate for the structure of ΔENAC have been deposited in the EMDataBank and Protein Data Bank under the accession codes EMD-7130 and 6BQN, respectively.

The following datasets were generated:

Author(s)	Year	Dataset title	Dataset URL	Database, license, and accessibility information
Noreng S, Bharadwaj A, Posert R, Yoshioka C, Baconguis I	2018	ΔENaC model coordinates	https://www.rcsb.org/structure/6BQN	Publicly available at RCSB Protein Data Bank (accession no. 6BQN)
Noreng S, Bharadwaj A, Posert R, Yoshioka C, Baconguis I	2018	ΔENaC map, FSC	http://emsearch.rutgers.edu/atlas/7130_summary.html	Publicly available at the Electron Microscopy Data Bank (accession no. EMD-7130)

References

Adams PD, Afonine PV, Bunkóczi G, Chen VB, Echols N, Headd JJ, Hung LW, Jain S, Kapral GJ, Grosse Kunstleve RW, McCoy AJ, Moriarty NW, Oeffner RD, Read RJ, Richardson DC, Richardson JS, Terwilliger TC, Zwart PH. 2011. The Phenix software for automated determination of macromolecular structures. *Methods* **55**: 94–106. DOI: https://doi.org/10.1016/j.ymeth.2011.07.005, PMID: 21821126

Arnold K, Bordoli L, Kopp J, Schwede T. 2006. The SWISS-MODEL workspace: a web-based environment for protein structure homology modelling. *Bioinformatics* **22**:195–201. DOI: https://doi.org/10.1093/bioinformatics/bti770, PMID: 16301204

Baconguis I, Gouaux E. 2012. Structural plasticity and dynamic selectivity of acid-sensing ion channel-spider toxin complexes. *Nature* **489**:400–405. DOI: https://doi.org/10.1038/nature11375, PMID: 22842900

Baconguis I, Bohlen CJ, Goehring A, Julius D, Gouaux E. 2014. X-ray structure of acid-sensing ion channel 1-snake toxin complex reveals open state of a Na(+)-selective channel. *Cell* **156**:717–729. DOI: https://doi.org/10.1016/j.cell.2014.01.011, PMID: 24507937

Bruns JB, Carattino MD, Sheng S, Maarouf AB, Weisz OA, Pilewski JM, Hughey RP, Kleyman TR. 2007. Epithelial na+ channels are fully activated by furin- and prostasin-dependent release of an inhibitory peptide from the gamma-subunit. *Journal of Biological Chemistry* **282**:6153–6160. DOI: https://doi.org/10.1074/jbc.M610636200, PMID: 17199078

Buchan DW, Minneci F, Nugent TC, Bryson K, Jones DT. 2013. Scalable web services for the PSIPRED protein analysis workbench. *Nucleic Acids Research* **41**:W349–W357. DOI: https://doi.org/10.1093/nar/gkt381, PMID: 23748958

Büsst CJ. 2013. Blood pressure regulation via ENaC: from gene to kidney and beyond. *Clinical and Experimental Pharmacology and Physiology, N/a-N/a* **40**:495–503. DOI: https://doi.org/10.1111/1440-1681.12124

Caldwell RA, Boucher RC, Stutts MJ. 2004. Serine protease activation of near-silent epithelial na+ channels. *American Journal of Physiology. Cell Physiology* **286**:C190–C194. DOI: https://doi.org/10.1152/ajpcell.00342.2003, PMID: 12967915

Canessa CM, Horisberger JD, Rossier BC. 1993. Epithelial sodium channel related to proteins involved in neurodegeneration. *Nature* **361**:467–470. DOI: https://doi.org/10.1038/361467a0, PMID: 8381523

Canessa CM, Schild L, Buell G, Thorens B, Gautschi I, Horisberger JD, Rossier BC. 1994. Amiloride-sensitive epithelial Na+ channel is made of three homologous subunits. *Nature* **367**:463–467. DOI: https://doi.org/10.1038/367463a0, PMID: 8107805

Carattino MD, Sheng S, Bruns JB, Pilewski JM, Hughey RP, Kleyman TR. 2006. The epithelial na+ channel is inhibited by a peptide derived from proteolytic processing of its alpha subunit. *The Journal of Biological Chemistry* **281**:18901–18907. DOI: https://doi.org/10.1074/jbc.M604109200, PMID: 16690613

Carattino MD, Hughey RP, Kleyman TR. 2008a. Proteolytic processing of the epithelial sodium channel gamma subunit has a dominant role in channel activation. *Journal of Biological Chemistry* **283**:25290–25295. DOI: https://doi.org/10.1074/jbc.M803931200, PMID: 18650438

Carattino MD, Passero CJ, Steren CA, Maarouf AB, Pilewski JM, Myerburg MM, Hughey RP, Kleyman TR. 2008b. Defining an inhibitory domain in the alpha-subunit of the epithelial sodium channel. *American Journal of Physiology-Renal Physiology* **294**:F47–F52. DOI: https://doi.org/10.1152/ajprenal.00399.2007, PMID: 18032549

Chalfie M, Wolinsky E. 1990. The identification and suppression of inherited neurodegeneration in Caenorhabditis elegans. *Nature* **345**:410–416. DOI: https://doi.org/10.1038/345410a0, PMID: 2342572

Chang SS, Grunder S, Hanukoglu A, Rösler A, Mathew PM, Hanukoglu I, Schild L, Lu Y, Shimkets RA, Nelson-Williams C, Rossier BC, Lifton RP. 1996. Mutations in subunits of the epithelial sodium channel cause salt wasting with hyperkalaemic acidosis, pseudohypoaldosteronism type 1. *Nature Genetics* **12**:248–253. DOI: https://doi.org/10.1038/ng0396-248, PMID: 8589714

Chelur DS, Ernstrom GG, Goodman MB, Yao CA, Chen L, O' Hagan R, Chalfie M. 2002. The mechanosensory protein MEC-6 is a subunit of the C. elegans touch-cell degenerin channel. *Nature* **420**:669–673. DOI: https://doi.org/10.1038/nature01205, PMID: 12478294

Chen VB, Arendall WB, Headd JJ, Keedy DA, Immormino RM, Kapral GJ, Murray LW, Richardson JS, Richardson DC. 2010. MolProbity: all-atom structure validation for macromolecular crystallography. *Acta Crystallographica Section D Biological Crystallography* **66**:12–21. DOI: https://doi.org/10.1107/S0907444909042073, PMID: 20057044

Chen J, Myerburg MM, Passero CJ, Winarski KL, Sheng S. 2011. External Cu2+ inhibits human epithelial na+ channels by binding at a subunit interface of extracellular domains. *The Journal of Biological Chemistry* **286**:27436–27446. DOI: https://doi.org/10.1074/jbc.M111.232058, PMID: 21659509

Collier DM, Snyder PM. 2011. Identification of epithelial na+ channel (ENaC) intersubunit cl- inhibitory residues suggests a trimeric alpha gamma beta channel architecture. *The Journal of Biological Chemistry* **286**:6027–6032. DOI: https://doi.org/10.1074/jbc.M110.198127, PMID: 21149458

Collier DM, Tomkovicz VR, Peterson ZJ, Benson CJ, Snyder PM. 2014. Intersubunit conformational changes mediate epithelial sodium channel gating. *The Journal of General Physiology* **144**:337–348. DOI: https://doi.org/10.1085/jgp.201411208, PMID: 25225551

Cottrell GA, Green KA, Davies NW. 1990. The neuropeptide Phe-Met-Arg-Phe-NH2 (FMRFamide) can activate a ligand-gated ion channel in Helix neurones. *Pflügers Archiv European Journal of Physiology* **416**:612–614. DOI: https://doi.org/10.1007/BF00382698, PMID: 1700364

DiMaio F, Leaver-Fay A, Bradley P, Baker D, André I. 2011. Modeling symmetric macromolecular structures in Rosetta3. *PLOS ONE* **6**:e20450. DOI: https://doi.org/10.1371/journal.pone.0020450, PMID: 21731614

Driscoll M, Chalfie M. 1991. The mec-4 gene is a member of a family of Caenorhabditis elegans genes that can mutate to induce neuronal degeneration. *Nature* **349**:588–593. DOI: https://doi.org/10.1038/349588a0, PMID: 1672038

Drozdetskiy A, Cole C, Procter J, Barton GJ. 2015. JPred4: a protein secondary structure prediction server. *Nucleic Acids Research* **43**:W389–W394. DOI: https://doi.org/10.1093/nar/gkv332, PMID: 25883141

Edelheit O, Hanukoglu I, Gizewska M, Kandemir N, Tenenbaum-Rakover Y, Yurdakök M, Zajaczek S, Hanukoglu A. 2005. Novel mutations in epithelial sodium channel (ENaC) subunit genes and phenotypic expression of multisystem pseudohypoaldosteronism. *Clinical Endocrinology* **62**:547–553. DOI: https://doi.org/10.1111/j.1365-2265.2005.02255.x, PMID: 15853823

Emsley P, Cowtan K. 2004. Coot: model-building tools for molecular graphics. *Acta Crystallographica. Section D, Biological Crystallography* **60**:2126–2132. DOI: https://doi.org/10.1107/S0907444904019158, PMID: 15572765

Garty H, Palmer LG. 1997. Epithelial sodium channels: function, structure, and regulation. *Physiological Reviews* **77**:359–396. DOI: https://doi.org/10.1152/physrev.1997.77.2.359, PMID: 9114818

Goehring A, Lee CH, Wang KH, Michel JC, Claxton DP, Baconguis I, Althoff T, Fischer S, Garcia KC, Gouaux E. 2014. Screening and large-scale expression of membrane proteins in mammalian cells for structural studies. *Nature Protocols* **9**:2574–2585. DOI: https://doi.org/10.1038/nprot.2014.173, PMID: 25299155

Grant T, Rohou A, Grigorieff N. 2018. cisTEM, user-friendly software for single-particle image processing. *eLife* **7**:e35383. DOI: https://doi.org/10.7554/eLife.35383, PMID: 29513216

Gründer S, Firsov D, Chang SS, Jaeger NF, Gautschi I, Schild L, Lifton RP, Rossier BC. 1997. A mutation causing pseudohypoaldosteronism type 1 identifies a conserved glycine that is involved in the gating of the epithelial sodium channel. *The EMBO Journal* **16**:899–907. DOI: https://doi.org/10.1093/emboj/16.5.899, PMID: 9118951

Hamm LL, Feng Z, Hering-Smith KS. 2010. Regulation of sodium transport by ENaC in the kidney. *Current Opinion in Nephrology and Hypertension* **19**:98–105. DOI: https://doi.org/10.1097/MNH.0b013e328332bda4, PMID: 19996890

Hansson JH, Nelson-Williams C, Suzuki H, Schild L, Shimkets R, Lu Y, Canessa C, Iwasaki T, Rossier B, Lifton RP. 1995. Hypertension caused by a truncated epithelial sodium channel gamma subunit: genetic heterogeneity of liddle syndrome. *Nature Genetics* **11**:76–82. DOI: https://doi.org/10.1038/ng0995-76, PMID: 7550319

Hanukoglu I, Hanukoglu A. 2016. Epithelial sodium channel (ENaC) family: Phylogeny, structure-function, tissue distribution, and associated inherited diseases. *Gene* **579**:95–132 . DOI: https://doi.org/10.1016/j.gene.2015.12.061, PMID: 26772908

Heymann JB, Belnap DM. 2007. Bsoft: image processing and molecular modeling for electron microscopy. *Journal of Structural Biology* **157**:3–18. DOI: https://doi.org/10.1016/j.jsb.2006.06.006, PMID: 17011211

Hughey RP, Mueller GM, Bruns JB, Kinlough CL, Poland PA, Harkleroad KL, Carattino MD, Kleyman TR. 2003. Maturation of the epithelial na+ channel involves proteolytic processing of the alpha- and gamma-subunits. *The Journal of Biological Chemistry* **278**:37073–37082. DOI: https://doi.org/10.1074/jbc.M307003200, PMID: 12871941

Hughey RP, Bruns JB, Kinlough CL, Harkleroad KL, Tong Q, Carattino MD, Johnson JP, Stockand JD, Kleyman TR. 2004. Epithelial sodium channels are activated by furin-dependent proteolysis. *Journal of Biological Chemistry* **279**:18111–18114. DOI: https://doi.org/10.1074/jbc.C400080200, PMID: 15007080

Ismailov II, Awayda MS, Jovov B, Berdiev BK, Fuller CM, Dedman JR, Kaetzel M, Benos DJ. 1996. Regulation of epithelial sodium channels by the cystic fibrosis transmembrane conductance regulator. *The Journal of Biological Chemistry* **271**:4725–4732. DOI: https://doi.org/10.1074/jbc.271.9.4725, PMID: 8617738

Jasti J, Furukawa H, Gonzales EB, Gouaux E. 2007. Structure of acid-sensing ion channel 1 at 1.9 A resolution and low pH. *Nature* **449**:316–323. DOI: https://doi.org/10.1038/nature06163, PMID: 17882215

Kashlan OB, Boyd CR, Argyropoulos C, Okumura S, Hughey RP, Grabe M, Kleyman TR. 2010. Allosteric inhibition of the epithelial na+ channel through peptide binding at peripheral finger and thumb domains. *Journal of Biological Chemistry* **285**:35216–35223. DOI: https://doi.org/10.1074/jbc.M110.167064, PMID: 20817728

Kashlan OB, Blobner BM, Zuzek Z, Carattino MD, Kleyman TR. 2012. Inhibitory tract traps the epithelial na+ channel in a low activity conformation. *The Journal of Biological Chemistry* **287**:20720–20726. DOI: https://doi.org/10.1074/jbc.M112.358218, PMID: 22511777

Kashlan OB, Blobner BM, Zuzek Z, Tolino M, Kleyman TR. 2015. Na+ inhibits the epithelial na+ channel by binding to a site in an extracellular acidic cleft. *The Journal of Biological Chemistry* **290**:568–576. DOI: https://doi.org/10.1074/jbc.M114.606152, PMID: 25389295

Kawate T, Gouaux E. 2006. Fluorescence-detection size-exclusion chromatography for precrystallization screening of integral membrane proteins. *Structure* **14**:673–681. DOI: https://doi.org/10.1016/j.str.2006.01.013, PMID: 16615909

Kellenberger S, Schild L. 2002. Epithelial sodium channel/degenerin family of ion channels: a variety of functions for a shared structure. *Physiological Reviews* **82**:735–767. DOI: https://doi.org/10.1152/physrev.00007.2002, PMID: 12087134

Kerem E, Bistritzer T, Hanukoglu A, Hofmann T, Zhou Z, Bennett W, MacLaughlin E, Barker P, Nash M, Quittell L, Boucher R, Knowles MR. 1999. Pulmonary epithelial sodium-channel dysfunction and excess airway liquid in pseudohypoaldosteronism. *New England Journal of Medicine* **341**:156–162. DOI: https://doi.org/10.1056/NEJM199907153410304, PMID: 10403853

Kleyman TR, Carattino MD, Hughey RP. 2009. ENaC at the cutting edge: regulation of epithelial sodium channels by proteases. *Journal of Biological Chemistry* **284**:20447–20451. DOI: https://doi.org/10.1074/jbc.R800083200, PMID: 19401469

Krishtal OA, Pidoplichko VI. 1981. A receptor for protons in the membrane of sensory neurons may participate in nociception. *Neuroscience* **6**:2599–2601. DOI: https://doi.org/10.1016/0306-4522(81)90105-6, PMID: 6275299

Lingueglia E, Champigny G, Lazdunski M, Barbry P. 1995. Cloning of the amiloride-sensitive FMRFamide peptide-gated sodium channel. *Nature* **378**:730–733. DOI: https://doi.org/10.1038/378730a0, PMID: 7501021

Mastronade DN. 2003. SerialEM: A Program for Automated Tilt Series Acquisition on Tecnai Microscopes Using Prediction of Specimen Position. *Microscopy and Microanalysis* **9**:1182–1183.

McDonald FJ, Snyder PM, McCray PB, Welsh MJ. 1994. Cloning, expression, and tissue distribution of a human amiloride-sensitive na+ channel. *The American Journal of Physiology* **266**:L728–L734. DOI: https://doi.org/10.1152/ajplung.1994.266.6.L728, PMID: 8023962

Orce GG, Castillo GA, Margolius HS. 1980. Inhibition of short-circuit current in toad urinary bladder by inhibitors of glandular kallikrein. *The American Journal of Physiology* **239**:F459–F465. DOI: https://doi.org/10.1152/ajprenal.1980.239.5.F459, PMID: 6159795

Passero CJ, Carattino MD, Kashlan OB, Myerburg MM, Hughey RP, Kleyman TR. 2010. Defining an inhibitory domain in the gamma subunit of the epithelial sodium channel. *American Journal of Physiology-Renal Physiology* **299**:F854–F861. DOI: https://doi.org/10.1152/ajprenal.00316.2010, PMID: 20630937

Pettersen EF, Goddard TD, Huang CC, Couch GS, Greenblatt DM, Meng EC, Ferrin TE. 2004. UCSF chimera–a visualization system for exploratory research and analysis. *Journal of Computational Chemistry* **25**:1605–1612. DOI: https://doi.org/10.1002/jcc.20084, PMID: 15264254

Punjani A, Rubinstein JL, Fleet DJ, Brubaker MA. 2017. cryoSPARC: algorithms for rapid unsupervised cryo-EM structure determination. *Nature Methods* **14**:290–296. DOI: https://doi.org/10.1038/nmeth.4169, PMID: 28165473

Rossier BC, Stutts MJ. 2009. Activation of the epithelial sodium channel (ENaC) by serine proteases. *Annual Review of Physiology* **71**:361–379. DOI: https://doi.org/10.1146/annurev.physiol.010908.163108, PMID: 1892 8407

Rossier BC, Baker ME, Studer RA. 2015. Epithelial sodium transport and its control by aldosterone: the story of our internal environment revisited. *Physiological Reviews* **95**:297–340. DOI: https://doi.org/10.1152/physrev. 00011.2014, PMID: 25540145

Salih M, Gautschi I, van Bemmelen MX, Di Benedetto M, Brooks AS, Lugtenberg D, Schild L, Hoorn EJ. 2017. A Missense Mutation in the Extracellular Domain of αENaC Causes Liddle Syndrome. *Journal of the American Society of Nephrology : JASN* **28**:3291–3299. DOI: https://doi.org/10.1681/ASN.2016111163, PMID: 28710092

Scheres SH. 2012. RELION: implementation of a bayesian approach to cryo-EM structure determination. *Journal of Structural Biology* **180**:519–530. DOI: https://doi.org/10.1016/j.jsb.2012.09.006, PMID: 23000701

Shimkets RA, Warnock DG, Bositis CM, Nelson-Williams C, Hansson JH, Schambelan M, Gill JR, Ulick S, Milora RV, Findling JW. 1994. Liddle's syndrome: heritable human hypertension caused by mutations in the beta subunit of the epithelial sodium channel. *Cell* **79**:407–414. DOI: https://doi.org/10.1016/0092-8674(94)90250-X, PMID: 7954808

Shobair M, Dagliyan O, Kota P, Dang YL, He H, Stutts MJ, Dokholyan NV. 2016. Gain-of-Function mutation W493R in the epithelial sodium channel allosterically reconfigures intersubunit coupling. *Journal of Biological Chemistry* **291**:3682–3692. DOI: https://doi.org/10.1074/jbc.M115.678052, PMID: 26668308

Soundararajan R, Pearce D, Hughey RP, Kleyman TR. 2010. Role of epithelial sodium channels and their regulators in hypertension. *Journal of Biological Chemistry* **285**:30363–30369. DOI: https://doi.org/10.1074/jbc. R110.155341, PMID: 20624922

Stockand JD, Staruschenko A, Pochynyuk O, Booth RE, Silverthorn DU. 2008. Insight toward epithelial na+ channel mechanism revealed by the acid-sensing ion channel 1 structure. *IUBMB Life* **60**:620–628. DOI: https:// doi.org/10.1002/iub.89, PMID: 18459164

Vallet V, Chraibi A, Gaeggeler HP, Horisberger JD, Rossier BC. 1997. An epithelial serine protease activates the amiloride-sensitive sodium channel. *Nature* **389**:607–610. DOI: https://doi.org/10.1038/39329, PMID: 9335501

Vallet V, Pfister C, Loffing J, Rossier BC. 2002. Cell-surface expression of the channel activating protease xCAP-1 is required for activation of ENaC in the xenopus oocyte. *Journal of the American Society of Nephrology : JASN* **13**:588–594. PMID: 11856761

Voss NR, Yoshioka CK, Radermacher M, Potter CS, Carragher B. 2009. DoG picker and TiltPicker: software tools to facilitate particle selection in single particle electron microscopy. *Journal of Structural Biology* **166**:205–213. DOI: https://doi.org/10.1016/j.jsb.2009.01.004, PMID: 19374019

Vuagniaux G, Vallet V, Jaeger NF, Hummler E, Rossier BC. 2002. Synergistic activation of ENaC by three membrane-bound channel-activating serine proteases (mCAP1, mCAP2, and mCAP3) and serum- and glucocorticoid-regulated kinase (Sgk1) in xenopus oocytes. *The Journal of General Physiology* **120**:191–201. DOI: https://doi.org/10.1085/jgp.20028598, PMID: 12149280

Vullo S, Bonifacio G, Roy S, Johner N, Bernèche S, Kellenberger S. 2017. Conformational dynamics and role of the acidic pocket in ASIC pH-dependent gating. *PNAS* **114**:3768. DOI: https://doi.org/10.1073/pnas. 1620560114, PMID: 28320963

Waldmann R, Champigny G, Bassilana F, Heurteaux C, Lazdunski M. 1997a. A proton-gated cation channel involved in acid-sensing. *Nature* **386**:173–177. DOI: https://doi.org/10.1038/386173a0, PMID: 9062189

Waldmann R, Bassilana F, de Weille J, Champigny G, Heurteaux C, Lazdunski M. 1997b. Molecular cloning of a non-inactivating proton-gated na+ channel specific for sensory neurons. *The Journal of Biological Chemistry* **272**:20975–20978. PMID: 9261094

Xu D, Zhang Y. 2012. Ab initio protein structure assembly using continuous structure fragments and optimized knowledge-based force field. *Proteins* **80**:1715–1735. DOI: https://doi.org/10.1002/prot.24065, PMID: 22411565

Zhang K. 2016. Gctf: real-time CTF determination and correction. *Journal of Structural Biology* **193**:1–12. DOI: https://doi.org/10.1016/j.jsb.2015.11.003, PMID: 26592709

Zheng H, Liu X, Sharma NM, Li Y, Pliquett RU, Patel KP. 2016. Urinary Proteolytic Activation of Renal Epithelial Na+ Channels in Chronic Heart Failure. *Hypertension* **67**:197–205. DOI: https://doi.org/10.1161/ HYPERTENSIONAHA.115.05838, PMID: 26628676

Zheng SQ, Palovcak E, Armache JP, Verba KA, Cheng Y, Agard DA. 2017. MotionCor2: anisotropic correction of beam-induced motion for improved cryo-electron microscopy. *Nature Methods* **14**:331–332. DOI: https://doi. org/10.1038/nmeth.4193, PMID: 28250466